

# Sensitivity of Real-Data Simulations of the 3 May 1999 Oklahoma City Tornadoic Supercell and Associated Tornadoes to Multimoment Microphysics. Part II: Analysis of Buoyancy and Dynamic Pressure Forces in Simulated Tornado-Like Vortices

DANIEL T. DAWSON II\*

*Center for Analysis and Prediction of Storms, University of Oklahoma, Norman, Oklahoma*

MING XUE AND ALAN SHAPIRO

*Center for Analysis and Prediction of Storms, and School of Meteorology, University of Oklahoma, Norman, Oklahoma*

JASON A. MILBRANDT

*Atmospheric Numerical Prediction Research, Environment Canada, Montreal, Quebec, Canada*

ALEXANDER D. SCHENKMAN

*Center for Analysis and Prediction of Storms, University of Oklahoma, Norman, Oklahoma*

(Manuscript received 20 April 2015, in final form 19 November 2015)

## ABSTRACT

Vortex stretching by intense upward accelerations is a critical process for tornadogenesis and maintenance. Two high-resolution (250-m grid spacing) real-data simulations of the 3 May 1999 Oklahoma City, Oklahoma, supercell and associated tornadoes, using single- and triple-moment microphysics parameterization schemes, respectively, are examined. Microphysical, thermodynamic, and dynamic impacts on the vertical accelerations near and within simulated tornado-like vortices (TLVs) are analyzed. Systematic differences in behavior of the TLVs between the two experiments are found; the TLV in the triple-moment simulation is substantially more intense and longer lived than in the single-moment case. The triple-moment scheme in this case produces less rain and hail mass in the low levels and drop size distributions of rain shifted toward larger drops, relative to the single-moment scheme, leading to less latent cooling and warmer outflow. Trajectory analyses reveal that more parcels entering the TLV in the triple-moment simulation have a history of dynamically induced descent, whereas buoyantly driven descent is more prevalent in the single-moment experiment. It is found that the intensity and longevity of the TLV are tied to weaker negative or neutral thermal buoyancy in the air flowing into the TLV in the triple-moment case, consistent with previous observational and modeling studies. Finally, the contribution to buoyancy from pressure perturbations is found to be of prime importance within the TLV, where strong negative pressure perturbations lead to substantial positive buoyancy. This contribution compensates for the slight negative thermal buoyancy and negative dynamic pressure gradient acceleration in the triple-moment case.

---

\* Current affiliation: Department of Earth, Atmospheric, and Planetary Sciences, Purdue University, West Lafayette, Indiana.

---

*Corresponding author address:* Dr. Daniel T. Dawson II, Department of Earth, Atmospheric, and Planetary Sciences, Purdue University, 550 Stadium Mall Dr., West Lafayette, IN 47907.  
E-mail: dandawson@purdue.edu

## 1. Introduction

The possibility that the thermodynamic characteristics of tornado inflow air may have a substantial impact on supercell tornadogenesis and tornado maintenance has been recognized for some time (Ludlam 1963). Leslie and Smith (1978) performed axially symmetric idealized simulations of vortices stretched by an imposed updraft aloft

and imposed swirl velocity on the cylindrical boundary and investigated the effect of increasing low-level static stability on the development of concentrated near-ground rotation. They found that as static stability (and therefore negative buoyancy for upward-displaced parcels) increased, near-ground rotation was progressively inhibited.

Markowski et al. (2003) performed similar simulations in which a rotating updraft was imposed aloft, but with no initial rotation in the low levels. They imposed an annular source of rainwater at some distance above the surface (analogous to a hook echo in a real supercell) that allowed for a downdraft to form, via the effects of precipitation loading and evaporative cooling, leading to a negatively buoyant near-surface cold pool. They found that with greater precipitation concentrations tornado-genesis was suppressed owing in part to the negative buoyancy directly opposing upward vertical stretching of the incipient tornado and the associated radial convergence of near-surface air toward the axis of rotation.

Parker (2012) performed axisymmetric simulations featuring an initial mesocyclone and heat source aloft in thermodynamic environments characterized by differing temperature lapse rates. He found that environments with neutral lapse rates facilitated downward transport of angular momentum to the surface, resulting in the development of a surface vortex. However, stably stratified environments impeded downward momentum transport, instead exciting gravity waves that transported energy away from the storm; no surface vortex formed in these cases.

Markowski and Richardson (2014) performed idealized pseudostorm experiments in which a fixed positive (negative) buoyancy source to represent a supercell storm updraft (downdraft) was placed in environments of varying low-level shear. Their results were consistent with those of Markowski et al. (2003) in that those experiments with a stronger (weaker) fixed negative buoyancy source and the resulting colder outflow were associated with the development of weaker (stronger) near-surface vortices.

Snook and Xue (2008) performed 3D idealized simulations of tornadoes within their parent supercell storms with differing values of the (fixed) intercept parameters of rain and hail within a single-moment bulk microphysics scheme. They found that configurations favoring relatively small raindrops and hailstones produced stronger cold pools and weaker or nonexistent tornado-like vortices (TLVs)<sup>1</sup> as opposed to the

configurations that favored large raindrops and hailstones which produced stronger, longer-lived TLVs. These studies varied as to the origin of the inflow air into the simulated TLVs: in Leslie and Smith (1978) and Parker (2012), the emphasis was on the thermodynamic stability characteristics of the “undisturbed” environment, while in Markowski et al. (2003), Snook and Xue (2008), and Markowski and Richardson (2014) the primary source of TLV inflow was evaporatively cooled air that originated in the storm (or imposed) downdraft. However, these and other studies are in good agreement that tornadoes are negatively (positively) impacted by the ingestion of negatively buoyant or more stable air.

Finally, Naylor and Gilmore (2014) performed several high-resolution (100-m grid spacing) simulations of both tornadic and nontornadic supercells. Their results contrasted with those of prior modeling studies: the tornadic supercells tended to have stronger cold pools than their nontornadic counterparts. The fact that the simulations in their study were initialized in widely varying environments is one plausible explanation of this discrepancy; in particular, their tornadic simulations were systematically characterized by substantially higher CAPE and lower LFCs than the nontornadic simulations. This difference led to stronger low-level updrafts and associated vertical stretching of vorticity, but also correspondingly stronger and colder downdrafts and outflow, in the tornadic cases. In contrast, the aforementioned studies either utilized a single environmental sounding or otherwise specified fixed artificial storm-scale updraft forcing mechanisms, effectively removing this particular source of variability. Naylor and Gilmore (2014) also point out that these strong cold pools may have been exacerbated by their use of a single-moment bulk microphysics scheme with default values of the intercept parameters as in Gilmore et al. (2004).

Observations of the low-level thermodynamic properties of environmental air near supercells, both in outflow and inflow, have generally been limited, owing to the small scale of these storms relative to the spacing of traditional fixed surface observing stations. Mobile mesonet (Straka et al. 1996) thermodynamic observations in and around supercells were one of the tasks of both the original Verification of the Origin of Rotation in Tornadoes Experiment (VORTEX; spring 1994 and 1995) and VORTEX2 in the springs of 2009 and 2010 (Richardson et al. 2010). Markowski et al. (2002), Markowski (2002), and Shabbott and Markowski (2006) reported on mobile mesonet datasets acquired in several supercells both during and after VORTEX and found that, in agreement with most of the numerical

---

<sup>1</sup> Here, “tornado-like vortex” refers, as in Schenkman et al. (2012) and Part I, to a numerically simulated vortex that is not fully resolved in terms of internal circulations (such as the corner-flow region) but nevertheless has many of the characteristics of tornadoes.

simulations discussed above, tornadic supercells in general had smaller temperature and moisture deficits (relative to the inflow environment) in their cold pools than nontornadic supercells.

In this study, we investigate the impact of the thermodynamic characteristics of the near-tornado environment on the tornadic behavior of the 3 May 1999 Oklahoma City supercell through real-data numerical simulation experiments. In Dawson et al. (2015, hereafter Part I), high-resolution (nested grids with 3-km, 1-km, and 250-m horizontal grid spacing) numerical prediction experiments using single-, double-, and triple-moment (1M, 2M, and 3M, respectively) configurations of a multimoment bulk microphysics scheme were produced, from initial conditions that assimilated Doppler radar data as well as other high-resolution observations. We found that the 3M scheme overall performed the best, producing the smallest track errors for the mesocyclone on the 1-km grid and stronger and longer-lived TLVs on the 250-m grid, more comparable to the observed tornado. In contrast, the 1M scheme with the default Marshall and Palmer (1948) rain intercept parameter performed poorly, producing a cold pool that was too strong and only weak and short-lived TLVs. We analyzed in detail the differences in latent cooling from evaporation and melting among the schemes and how the differences led to different cold-pool intensities. Finally, we also discussed the general implications of such differences for tornado behavior.

In Part II of this study, we focus on understanding the dynamical and thermodynamical effects related to the very different behaviors of the TLVs in the different simulations. We analyze two of the above experiments: one utilizing the 3M microphysics scheme that exhibited weak cold pools and an intense long-track TLV and the other utilizing the 1M version of the same scheme that exhibited strong cold pools and relatively weak and short-lived TLVs. Extending the earlier findings obtained mostly based on observational and idealized simulations, this paper examines the relationship between cold-pool intensity and tornado behavior in a realistic, real data setting. More specifically, given that intense vertical stretching is the primary reason for rapid intensification and maintenance of near-surface vortices, we study the direct impacts of the buoyancy and dynamic pressure gradient forcing in the vertical momentum equation. We analyze carefully these quantities along trajectories that enter the TLVs near the ground and quantify their respective contributions to the vertical accelerations of those air parcels that lead directly to TLV intensification. Moreover, we diagnose the latent cooling associated with hydrometeor phase changes that

directly impact the buoyancy along these trajectories as well as other relevant quantities related to the hydro-meteor particle size distributions (PSDs).

In addition to the importance of the thermal component of the buoyancy, we find that the TLV itself provides an important positive contribution to the buoyancy forcing via the so-called pressure buoyancy term that enhances the magnitude of upward accelerations within the TLV. As far as we know, a quantitative analysis of the forcings responsible for rapid vertical acceleration and stretching leading to tornado vortex intensification has not been performed in the literature, at least not in the context of simulations of tornadoes (or TLVs) driven by real data. Finally, we wish to emphasize that we are deliberately setting aside the question of the ultimate source of vertical vorticity for the TLVs in order to focus solely on the vertical momentum budgets.

The rest of this paper is organized as follows. In section 2, after a brief summary of the simulations to be analyzed, we describe the methodology of the buoyancy diagnostics and trajectory analysis. Section 3 describes results of these analyses as applied to the tornadic region of the simulated supercell and describes the impacts on the intensity of the TLVs. We discuss the importance of the contribution to buoyancy forcing from pressure perturbations in Section 4. Finally, section 5 summarizes the study and discusses potential avenues for future work.

## 2. Methodology

### *a. Recapitulation of the 250-m simulations of the 3 May 1999 Oklahoma City tornado event*

In Part I, we presented data assimilation and forecasting experiments for the 3 May 1999 Oklahoma City, Oklahoma, tornadic supercell, using the Advanced Regional Prediction System (ARPS) model (Xue et al. 2001, 2003) with triply nested 3-km, 1-km, and 250-m grids and realistic underlying terrain. In this paper, we will focus on the 250-m grid simulations and briefly review their setup here. We performed four sets of nested experiments using different configurations of the Milbrandt and Yau (2005, hereafter the MY# scheme, where # refers to the number of moments predicted) multimoment bulk microphysics scheme. On the 1-km grid, radar data as well as other available observations were assimilated at 10-min intervals from 2100 to 2250 UTC, a period that covers the entire developing phase of tornadic supercell storms A and B and the early tornadic phase of storm A [based on the lettering and numbering convention of Speheger et al. (2002); see Fig. 1 and

Table 1 in Part I]. The 250-m experiments attempted to capture the evolution of near-tornado-scale circulations in free forecasts and were initialized from the interpolated 1-km forecasts of the same microphysics configurations at 2305 UTC. This time is about 20 min before the onset of the F5 Moore–Oklahoma City tornado in storm A, the primary focus of this paper.

Of the four 250-m experiments in Part I, we choose two for more detailed analysis in this paper: 250mMY1A and 250mMY3, and hereafter drop the leading “250m” for the sake of brevity. Experiment MY1A utilizes the SM version of the MY scheme, with a fixed intercept parameter for rain of  $8.0 \times 10^6 \text{ m}^{-4}$  [i.e., the well-known and widely used Marshall and Palmer (1948) value], while MY3 utilizes the full 3M version of the scheme, in which all three free parameters of the assumed gamma size distribution are allowed to vary independently. As shown in Part I, experiment MY1A produced overall smaller mean volume diameters of rain in the downdrafts, and correspondingly larger amounts of evaporative cooling, than MY3, and thus also produced stronger cold pools and only short-lived weak TLVs. Experiment MY3 produced the strongest and longest-lived TLV of all the experiments. Therefore, we focus on these two extreme cases and analyze in detail contributions of various components of the buoyancy and dynamic vertical pressure gradient forcings in the near-TLV region and their connections to the microphysics.

### b. Vertical momentum equation diagnostics

The anelastic vertical momentum equation in Lagrangian form with Coriolis force neglected can be written as

$$\frac{Dw}{Dt} = -\frac{1}{\bar{\rho}} \frac{\partial p'}{\partial z} + B + F, \quad (1)$$

where  $p'$  is the perturbation pressure relative to a horizontally homogeneous hydrostatic reference (or base) state with pressure  $\bar{p} = \bar{p}(z)$ , and  $\bar{\rho} = \bar{\rho}(z)$  is the density associated with the reference state. The first term on the right-hand side (rhs) represents the local vertical acceleration due to the vertical perturbation pressure gradient force (VPPGF). The second term  $B$  is the buoyancy, defined as

$$B \equiv -g \frac{\rho'}{\bar{\rho}}, \quad (2)$$

where  $\rho'$  is the perturbation density relative to the reference state  $\bar{\rho}$  and  $g$  is the acceleration due to gravity. Finally the last term  $F$  represents friction and other diffusive processes in the model, such as computational

and subgrid-scale turbulent mixing. Buoyancy  $B$  and the VPPGF are the two primary forcing terms in (1).

As discussed by Davies-Jones (2003, hereafter DJ03) and (Doswell and Markowski 2004, hereafter DM04), the partitioning of  $B$  and VPPGF in a continuous atmosphere is by no means trivial; the VPPGF in (1) generally contains contributions from both the flow dynamics and buoyancy in a manner that depends on the arbitrary choice of base state. As such, a proper decomposition of the vertical acceleration due to buoyancy on the one hand, and due to variations in the wind field on the other, is crucial for correct physical interpretation. Often,  $p'$  in (1) is divided into a part due solely to spatial variations in velocity (called the “dynamic pressure perturbation”)  $p'_d$  and a part due to the buoyancy field itself  $p'_b$  such that (1) can be rewritten as

$$\frac{Dw}{Dt} = -\frac{1}{\bar{\rho}} \frac{\partial p'_d}{\partial z} + \left( -\frac{1}{\bar{\rho}} \frac{\partial p'_b}{\partial z} + B \right) + F, \quad (3)$$

where the term in parentheses represents the total “buoyant contribution” (Emanuel 1994) to vertical accelerations that is independent of the specification of the base state, though its components are not (DJ03; DM04). Equation (3) and similar equations based on the perturbation Exner function have been used extensively in diagnostics of model convection simulations for many years.

Under the anelastic approximation, what DJ03 calls the “effective buoyancy”  $\beta$  (the Greek letter being used to distinguish it from the traditional buoyancy  $B$ ) can be derived from the solution of the Poisson equation:

$$-\nabla^2 \beta = g \nabla_H^2 \rho_T, \quad (4)$$

where  $\nabla^2$  and  $\nabla_H^2$  are the 3D and horizontal Laplacian operators, respectively, and  $\rho_T$  is the total “system” density of moist air plus suspended hydrometeors (assumed to be falling at their terminal velocities). The effective buoyancy  $\beta$  which depends solely on horizontal variations in the density field, is essentially the “static” part of the locally nonhydrostatic vertical pressure gradient force (NHVPGF; DJ03) and can be shown to be equivalent to the sum of the traditional buoyancy  $B$  and the part of the VPPGF associated with the buoyancy field. That is,  $\beta$  can be written as

$$\beta = \bar{\rho} \left( -\frac{1}{\bar{\rho}} \frac{\partial p'_b}{\partial z} + B \right), \quad (5)$$

where the term in parentheses is merely the buoyant contribution in the more traditional formulation of (3). Note that in (4) and (5),  $\beta$  is in units of force, whereas in our analyses, we present it in units of acceleration by

dividing through by the model base-state density  $\bar{\rho}$ . This is the same approach taken by Jeevanjee and Romps (2015). Similarly, we will refer to the VPPGF in terms of acceleration (i.e., the VPPGA).

While DJ03 provides an analytic solution to (4) using Green’s functions, we chose to solve (4) numerically by first discretizing it on the ARPS terrain-following grid and then solving it using a fast multigrid solver, mud3cr, in the MUDPACK (Adams 1989). Routine mud3cr was designed for arbitrary grid transformations that result in cross-derivative terms and variable scaling coefficients in the Laplacian operators of (4) (Adams and Smolarkiewicz 2001) and is therefore ideally suited for our purpose. Following DJ03, we specify homogeneous Dirichlet boundary conditions of  $\beta = 0$  for the bottom and top boundaries. This condition has often been used without rigorous justification in previous work; Jeevanjee and Romps (2015) show that this is the appropriate and unambiguous boundary condition based on their novel (but equivalent) definition of  $\beta$ . We also set lateral boundary conditions to the same homogenous Dirichlet conditions for faster convergence, as testing confirmed that the interior solution of  $\beta$  is relatively insensitive to the choice of either Dirichlet or Neumann conditions for these boundaries. Finally, after obtaining  $\beta$  from the numerical solution of (4), we calculate the dynamic VPPGA [term 2 on the rhs of (3), hereafter the DVPPGA] as a residual from the sum of the model diagnosed VPPGA and buoyancy terms [terms 2 and 3 on the rhs of (1)]. We found the frictional acceleration term in the vertical momentum equation from the model fields to be much smaller (not shown) than the other terms in (1). Therefore, we neglected this term for the purposes of this study.

While the above procedure produces analyses of buoyancy and DVPPGA that do not depend on the reference or base state, it is not immediately obvious how to separate out the influences of thermal, pressure, and hydrometeor perturbations to the total buoyant contribution with such an approach. When the density  $\rho$  is defined broadly to include the effects of hydrometeors (Emanuel 1994; DJ03), the buoyancy  $B$  can be written approximately (after neglecting higher-order terms) as

$$B \cong g \left( \frac{\theta'_v}{\bar{\theta}_v} - \frac{c_v}{c_p} \frac{p'}{\bar{p}} - q_{li} \right), \tag{6}$$

where  $\theta'_v$  and  $\bar{\theta}_v$  are the perturbation and base-state virtual potential temperature, respectively;  $c_v$  and  $c_p$  are the specific heats of dry air at constant volume and pressure, respectively; and  $q_{li}$  is the total hydrometeor ratio of liquid and ice species. The terms on the rhs of (6) are the contributions to  $B$  from potential temperature

and water vapor (hereafter the “thermal buoyancy” or  $B_{\theta_v}$ ), pressure (the “pressure buoyancy” or  $B_p$ ), and liquid and solid hydrometeor perturbations (“water loading” or  $B_q$ ), respectively. Analyses of the components of buoyancy utilizing a formulation similar to (6) are common in the literature.

Still, buoyancy  $B$  computed from (6) suffers from the aforementioned problem of base-state dependence and additionally from the fact that it depends only on the local values of the state variables. In contrast, the base-state-independent effective buoyancy  $\beta$  encapsulates the impact of both the local density perturbations and their extended spatial influence via the buoyancy-induced perturbation pressure gradient field [cf. (5)]. It is thus natural to ask if the separate influences of thermal, pressure, and hydrometeor effects on  $\beta$  can be computed in a manner similar to that for  $B$  in (6). To accomplish this decomposition, we first derive an approximate expression for moist air density  $\rho$  by utilizing the equation of state in the following form:

$$\rho = \frac{p_0^{R_d/c_p} p^{1-R_d/c_p}}{R_d \theta_v}, \tag{7}$$

where  $p_0$  is a reference pressure (typically 100 000 Pa) and  $R_d$  is the dry-air gas constant. We expand (7) around a hydrostatic base state and neglect higher-order terms to yield [see also Das (1979), (25)]

$$\rho \cong \bar{\rho} - \frac{\bar{\rho}}{\bar{\theta}_v} \theta'_v + \left( 1 - \frac{R_d}{c_p} \right) \frac{\bar{\rho}}{\bar{p}} p'. \tag{8}$$

Substituting this expression (where we are momentarily neglecting hydrometeor loading) into (4) yields

$$-\nabla^2 \beta \cong -g \frac{\bar{\rho}}{\bar{\theta}_v} \nabla_H^2 \theta'_v + g \left( 1 - \frac{R_d}{c_p} \right) \frac{\bar{\rho}}{\bar{p}} \nabla_H^2 p'. \tag{9}$$

One can then solve separately for the two terms on the rhs of (9) to yield the separate contributions from thermal (represented by variations in  $\theta_v$ ) and pressure effects on  $\beta$ , which we denote as  $\beta_{\theta_v}$  and  $\beta_p$ , respectively. Finally, to isolate the effects of hydrometeor loading, we again substitute the moist air density  $\rho$  for  $\rho_T$  on the rhs of (4) and subtract the result from the full  $\beta$  computed using (4), yielding the effective buoyancy due to hydrometeor loading  $\beta_q$ :

$$-\nabla^2 \beta_q = g \nabla_H^2 (\rho_T - \rho). \tag{10}$$

This decomposition procedure involves the reintroduction of a base state. Testing (not shown) revealed that the dependence of the individual terms in (9) on the

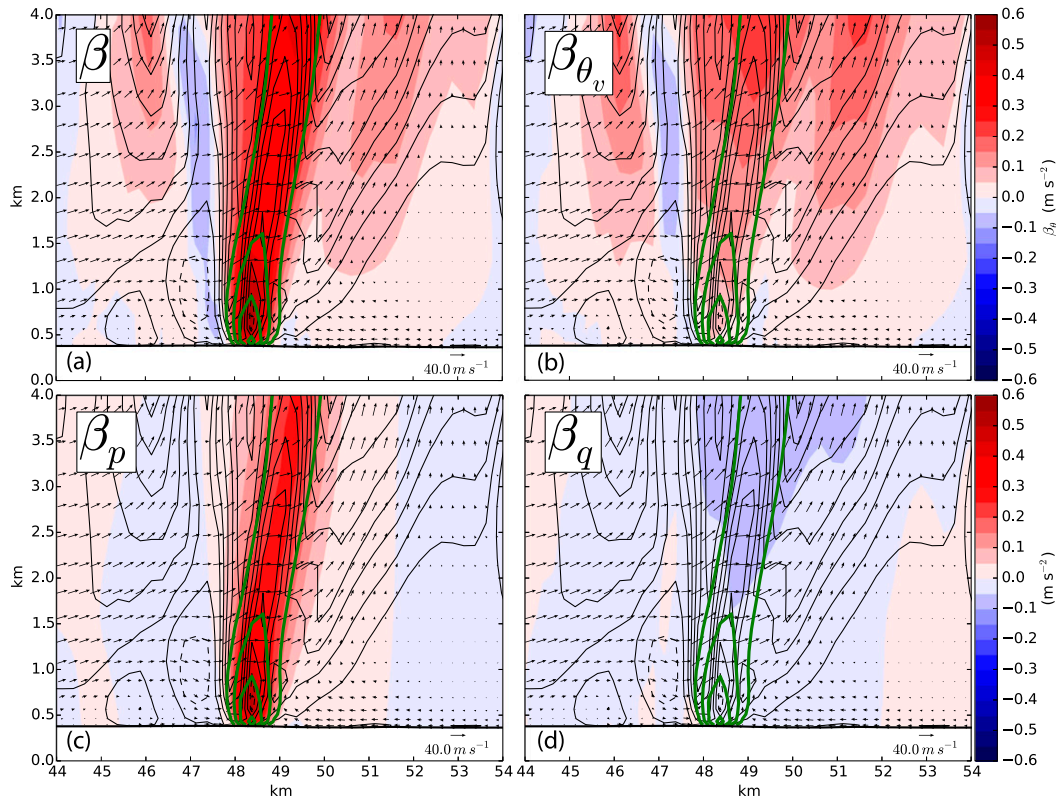


FIG. 1. North–south vertical cross section through the simulated TLV near its peak intensity at 4860 s in MY3. Shown in color fill are (a) total, (b) thermal, (c) pressure, and (d) hydrometeor loading effective buoyancy acceleration ( $\text{m s}^{-2}$ ). Overlaid in each panel are vertical velocity  $w$  (black contours,  $5 \text{ m s}^{-1}$ ) and vertical vorticity  $\zeta$  (green contours,  $0.01\text{-s}^{-1}$  increment, starting at  $0.01 \text{ s}^{-1}$ ).

choice of base state is relatively weak provided that  $\bar{\theta}_v$  and  $\bar{p}$  (and thus  $\bar{\rho}$ ) are chosen so that the perturbations from this base state are relatively small (the total  $\beta$  is of course still base-state independent). In idealized storm simulations, the base state is often defined by a single sounding and the perturbations are usually very small except for regions of active storms. In our real-data simulations, the model base state is instead defined as the horizontal average of the initial conditions. Because of the large horizontal inhomogeneity and significant evolution of the storm environment during the simulation, this model base state is often a poor choice for the reference state for the purposes of calculating the buoyancy. Observational convective storm studies such as Markowski et al. (2002) often compute the reference state as being some average of the storm inflow values, and this reference state can change in time as the inflow environment changes. In a similar vein, we compute a time-varying reference state by taking a horizontal average of  $\theta_v$ , utilizing an intermediate nonterrain-following Cartesian grid defined on a subdomain (not shown) of the full 250-m grid that encapsulates storm A

and its nearby environment. We obtain the new reference pressure  $\bar{p}$  by integrating the hydrostatic equation downward from the horizontally averaged full pressure at the model top. Finally, we interpolate the horizontally homogeneous reference fields from the Cartesian grid back to the model terrain-following grid and compute the perturbation variables as departures from this new reference state.

To demonstrate the foregoing decomposition of  $\beta$ , we plot in Fig. 1 north–south vertical cross sections through the TLV in MY3 at a time near its peak intensity for each of the individual components of  $\beta$ . The total  $\beta$  (Fig. 1a) is strongly positive within and near the TLV. By far the largest contribution to the total  $\beta$  in the vicinity of the simulated TLV comes from pressure variations ( $\beta_p$ , Fig. 1c). This is especially true in the low levels (below about 1 km AGL). We discuss the role and physical interpretation of  $\beta_p$  in more detail in section 4. Positive thermal buoyancy  $\beta_p$  increases steadily with height within the TLV as rising air parcels begin to realize their CAPE (Fig. 1b). Hydrometeor loading  $\beta_q$  (Fig. 1d) slightly opposes  $\beta_{\theta_v}$  in this region of the TLV.

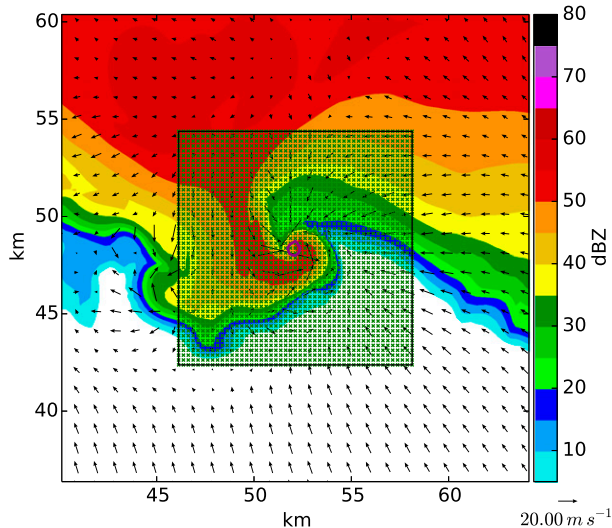


FIG. 2. Example of the trajectory analysis region centered on the TLV, as indicated by the black square inside the figure. Small green crosses indicate the initial points of the trajectories (every scalar grid point) at the given trajectory reference time (4860 s). Shown are surface reflectivity (dBZ, color shading), vertical vorticity  $\zeta$  (purple,  $0.1\text{-s}^{-1}$  contour shown), and ground-relative wind vectors placed every 1 km (scale in lower right), valid at 4860 s (0026 UTC 4 May 1999) for MY3.

### c. Trajectory analysis

We perform a trajectory-based analysis to investigate the thermodynamic and dynamic characteristics of the low-level air flowing into the simulated TLVs. Our approach is to initialize a grid of near-surface parcels at the first model level above ground where the vertical velocity is defined ( $\sim 20$  m AGL) and in a  $144\text{-km}^2$  square region surrounding the surface vortex at a given reference time. An example of the analysis region is shown in Fig. 2: a total of 2401 trajectories are initialized within the region. A new grid of trajectories is spawned at 30-s intervals throughout the forecast period in analysis regions that are recentered on the maximum surface vertical vorticity  $\zeta$  each time (the trajectory reference time). For each reference time, trajectories are integrated backward for 15 min and forward for 5 min, and various thermodynamic and dynamic quantities are interpolated to the trajectories. In particular, we examine the instantaneous microphysical latent cooling rates, the diagnosed  $\beta$  and DVPPGA, and several derived perturbation quantities. The initialization of trajectories on a regular grid also lends itself to convenient visualization. For example, an averaged or integrated quantity over some portion of a given trajectory can be plotted at the trajectory's location on the reference grid, allowing for spatial contouring of complex Lagrangian information on an Eulerian grid. The trajectories themselves

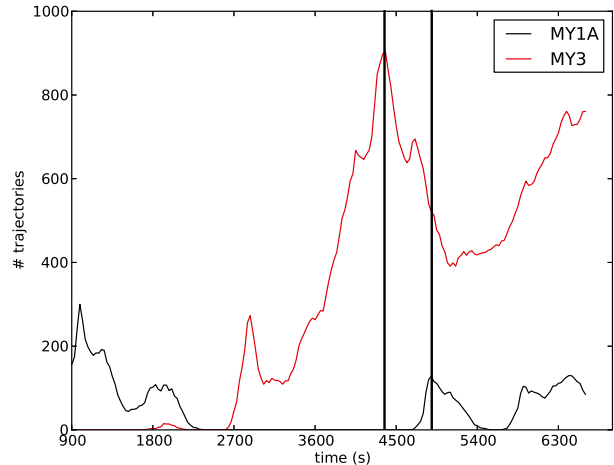


FIG. 3. Number of trajectories (out of a total of 2401) vs trajectory reference time that enter the TLV over the subsequent 5 min for MY1A (black) and MY3 (red). The vertical black bars highlight times when a relative maximum of trajectories entered the TLV at 4380 s for MY3 and 4890 s for MY1A, respectively.

are computed using model output at 30-s intervals and 2-s subtime steps. For each time step, a forward time integration is followed by a trapezoidal time integration. A similar trajectory program was used by Schenkman et al. (2012, 2014).

For convenience, we will call the forward and backward trajectory integration periods simply the forward and backward periods, respectively. To determine which parcels enter the tornado over the forward periods, we impose a criterion that the parcel must experience an instantaneous magnitude of  $\zeta \geq 0.1\text{ s}^{-1}$  at some time during the forward period (note, this criterion is not used to define the TLV itself but only to delineate trajectories that become part of the TLV flow). In this manner, the number of parcels that enter the TLV in the forward period out of the total in the  $144\text{-km}^2$  analysis region can be tracked in time (Fig. 3). This serves as a measure of the intensity of the TLV (a stronger TLV will generally ingest more near-surface air during a given time period). For other measures of the TLV intensity based on maximum horizontal wind speed and  $\zeta$ , we refer the reader to Fig. 18 in Part I. This approach allows for determining the main source regions of inflow parcels (at least those that are near the surface at the reference time) for the TLV and can illuminate changes in time and differences between simulations. Testing confirmed that while this criterion missed some trajectories that did enter the TLV, it did seem to effectively exclude trajectories that did not enter the TLV (such as those that encountered modest magnitudes of vorticity along the gust front). Thus, the fraction of trajectories entering the TLV shown in the analyses in the next section should

be considered as a conservative estimate. Finally, for each of those trajectories that enter the TLV in each of the 5-min forward periods, we determine the time at which the trajectory first enters the TLV (defined as when the instantaneous vertical vorticity first exceeds  $0.02 \text{ s}^{-1}$ ) and use this time to discriminate points outside the TLV from points within. For convenience we will define these time periods as the pre-TLV and intra-TLV periods, respectively.

### 3. Results

#### a. Trajectory footprints

The locations of trajectories that enter the TLV during the 5-min forward periods, when plotted at the reference time (when the trajectory points are on a regular grid), demarcate a 5-min “footprint” for the TLV. Figure 4 shows an example of the trajectory footprint as the region covered by open gray squares (where each square represents a single trajectory) for MY1A (left column) and MY3 (right column) at the time with the largest footprint (referred to as peak intensity) for both cases (black vertical bars in Fig. 3). The footprint is considerably larger in MY3 than in MY1A, commensurate with the more intense TLV in this experiment. Additionally, there are many more trajectories entering from the inflow region east and northeast of the TLV in the case of MY3.<sup>2</sup> Other times (not shown) show qualitatively similar behavior. Dahl et al. (2012) found that backward trajectories in the inflow region of the simulated supercell in their study were largely erroneous, even when wind fields were used every model time step, owing in part to rapid error growth for parcels in convergent flow (which becomes divergent in the backward time direction). There are two important differences in our trajectory analysis from those of Dahl et al. (2012). First, the trajectories in the inflow of the TLV are all at least partially forward in time, and indeed we use only the forward trajectories to define the TLV footprint (see above). As such, except for those trajectories very near the TLV at the reference time, the specific problem identified by Dahl et al. (2012) for backward trajectories does not apply. Second, our simulations contain surface friction, while those of Dahl et al. (2012)—as well as

most previous studies of this type—utilized free-slip lower boundary conditions. It is unknown how important this latter difference is to the modification of near-surface trajectories, but we speculate that near-surface inflow trajectories might be more prevalent when realistic surface friction is included owing to the associated greater radial convergence. Future work may examine this issue in more detail. Schenkman et al. (2014) also found trajectories coming from the inflow region in one of the developing simulated tornadoes in their study. However, in their case the representative trajectory was influenced by an incipient storm cell within the inflow of the main tornadic supercell and descended slightly (from  $\sim 70 \text{ m AGL}$ ) as it approached the tornado (see their Fig. 17), while in the present case no such history of descent is evident in the inflow trajectories. Finally, Naylor and Gilmore (2014) found inflow trajectories in several of their high-resolution idealized simulations of TLVs, and in two cases the low-level air entering the TLV contained no outflow trajectories. Both of these studies performed trajectory analyses focused on the time of tornadogenesis. Our results suggest that, at least once a mature TLV is established, downdraft air entering the TLV near ground level may not be as important as the relatively undisturbed near-surface inflow.

The initial height  $Z_{\text{init}}$  of each trajectory at the beginning of the 15-min backward period is shown in color shading in Figs. 4a,b for MY1A and MY3, respectively. Within the outflow, parcels tend to come from higher altitudes in MY1A than in MY3. This result is broadly consistent with the observational study of Markowski et al. (2002), who inferred higher parcel origin heights in the outflow of nontornadic storms as compared with tornadic storms. Additionally, there is substantially more variability in the initial parcel heights and associated outflow features in MY1A. In MY1A, there is a northward extension of trajectory points along a convergence boundary/region, perpendicular to which there is an east–west gradient in  $Z_{\text{init}}$  (Fig. 4a). In contrast, in MY3, the near-surface TLV inflow parcels come from a much broader and more symmetric region than MY1A (Fig. 4b), and the gradients in  $Z_{\text{init}}$  are much more subtle. Physically, this difference in geometry is consistent with the near-TLV flow in MY3 being dominated by broad and strong near-surface convergence as opposed to a greater role for the local vertical circulations associated with the surface boundaries in MY1A.

As also discussed in Part I, we note that the north–south convergence boundary in MY1A bears some resemblance to the “left-flank convergence boundary” (LFCB) found by Beck and Weiss (2013), in their high-resolution idealized supercell simulation, while this feature is muted or not present in MY3. In Beck and

<sup>2</sup>To test the impact of the temporal frequency of the data, we reran the MY3 experiment with a portion of the data output to disk at 5-s intervals instead of the 30-s intervals used in the analyses in this paper. Even with a factor-of-6 refinement in the temporal frequency of the data, we obtained the same qualitative results (not shown), indicating the robustness of the trajectory calculations herein.

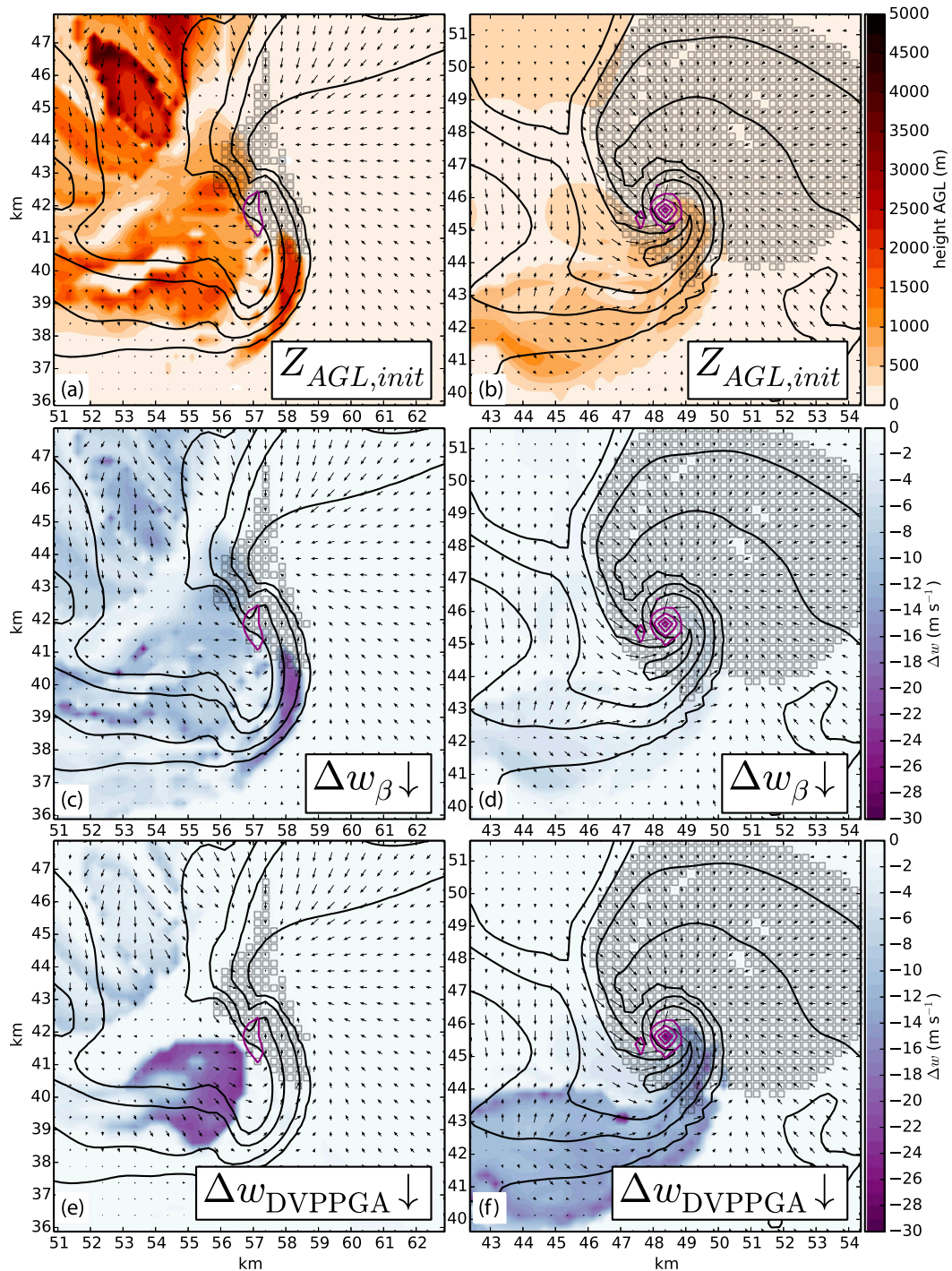


FIG. 4. Analysis (color shading) of (a),(b) initial trajectory height (m), (c),(d) integrated downward effective buoyancy  $\beta$  ( $\text{m s}^{-2}$ ), and (e),(f) integrated downward dynamic vertical perturbation pressure gradient acceleration (DVPPGA,  $\text{m s}^{-2}$ ) along trajectories at the trajectory reference time. The maximum height or integrated forcing is taken over the 15-min backward-trajectory integration period relative to the reference (panel) time at which the initial trajectory grid is defined. (left) MY1A at the reference time of 4890 s and (right) MY3 at 4380 s (cf. vertical black bars in Fig. 3). In each panel, the trajectories that enter the TLV in the subsequent 5-min forward period are denoted by light gray squares. Also overlaid in each panel are rainwater mixing ratio  $q_r$  (black contours; 0.01, 0.1, 0.5, 1.0, 5.0  $\text{g kg}^{-1}$  indicated), vertical vorticity  $\zeta$  (purple contours, every  $0.12 \text{ s}^{-1}$ , starting at  $0.03 \text{ s}^{-1}$ ) and ground-relative wind vectors at the first scalar point above ground ( $\sim 10 \text{ m}$ ), plotted every 500 m in the horizontal.

Weiss (2013), this boundary was also associated with gradients of  $\theta_e$  and initial parcel height, and their main simulation exhibited a relatively strong cold pool comparable to or stronger than that of MY1A in the current study. Finally, we speculate that the lack of a well-defined LFCB may be related to the relative dominance of inflow trajectories in MY3 (Fig. 4, right column); such a boundary might otherwise act as a “screen” blocking air from the inflow sector from reaching the TLV as appears to be the case in MY1A [Fig. 4, left column; see also Dahl et al. (2012), their Fig. 6]. Further investigation of this issue is beyond the scope of this study but may be investigated in future work.

In the bottom two rows of Fig. 4, the quantity in color shading represents, respectively, the integrated downward  $\beta$  and the integrated downward DVPPGA as experienced by the trajectories in the 15-min backward period. That is, for only those times when the net vertical acceleration (the sum of  $\beta$  and DVPPGA) was downward, the part of the acceleration due to  $\beta$  and DVPPGA, respectively, was integrated over the 15-min period. In this manner, the dominant forcing mechanisms for downward accelerations of the parcels as they descend toward the surface and reach their termination points on the reference grid can be visualized. A greater proportion of parcels in the outflow region in MY1A have been driven by negative buoyancy acceleration (Fig. 4c) as opposed to in MY3 (Fig. 4d), particularly in the northwest quadrant relative to the TLV center. In both cases, there is a region with a history of strong downward DVPPGA in the southwest quadrant (Figs. 4e,f), most of which does not interact directly with the TLV over the ensuing 5 min (cf. gray squares). However, in MY3, many of the parcels entering the TLV on the southeast side have had a history of strong downward DVPPGA (Fig. 4f). In contrast, from the same relative region in MY1A, most parcels have experienced predominantly negative buoyancy forcing (Fig. 4c). This basic pattern is apparent at other reference times (not shown).

#### b. Microphysical and vertical force analysis in the pre-TLV periods

Decomposing  $\beta$  into its components, we find that the greater negative  $\beta$  in MY1A is due to a combination of negative  $\beta_{\theta_v}$  and  $\beta_q$  (Figs. 5a and 5e, respectively). In Fig. 5 and subsequent similar plots, the positions of all TLV trajectories at 30-s intervals in the (15 min+) pre-TLV period are plotted as a function of the magnitude of a given quantity versus height. The solid black line indicates the average value of the quantity in 100-m height bins. Additionally, each trajectory point is colored by the quadrant it inhabits relative to the surface

location of the TLV at the reference time. For MY1A,  $\beta_{\theta_v}$  is negative on average for parcels at most heights in the pre-TLV period (Fig. 5a, black line), as is  $\beta_q$  (Fig. 5e). Virtually all of the parcels coming from above the surface originate in the southwest and northwest quadrants (relative to the location of the TLV at the reference time; green and red dots, respectively). In contrast, for MY3, the average  $\beta_{\theta_v}$  and  $\beta_q$  (Figs. 5b,f, respectively) are both small in magnitude, indicating that buoyancy is not a dominant forcing for downdraft parcels entering the TLV during this time period. In both cases, the effective pressure buoyancy  $\beta_p$  is relatively unimportant for parcels in the pre-TLV period (Figs. 5c and 5d, respectively).

At this point, it is worth discussing a curious and initially somewhat counterintuitive feature of  $\beta_q$  that can be seen particularly in the low levels in Fig. 5e: namely that for some points, the value of  $\beta_q$  is actually positive, despite the fact that the hydrometeor loading term  $B_q$  in the traditional buoyancy formulation [see (6)] is a negative semidefinite quantity. As intimated in section 2a, this can be understood as an effect of the extended influence of  $B_q$  by its induced pressure perturbation [first term in parentheses on the rhs of (5)]. This influence is implicit in the calculation of  $\beta_q$  from (10) and can be either positive or negative at a given location depending on the spatial variability of  $\rho_T - \rho$  and thus, ultimately,  $q_{li}$ . In short, regions of positive  $\beta_q$  can be viewed as resulting from the compensating (nondynamic) VPPGA induced by nearby areas of  $B_q$  and may be themselves hydrometeor free. To put it yet another way, parcels with low or zero  $q_{li}$  will typically have a density deficit relative to nearby parcels with higher  $q_{li}$  and thus may actually experience a net upward effective buoyancy force, depending on the details of the horizontal variation of the hydrometeor field. Similar arguments apply to the other components of  $\beta$ .

For the peak intensity reference times, TLV trajectories in MY1A on average have a history of smaller mean volume diameter  $D_{mr}$  of rainwater (Fig. 6a), larger rain-evaporation rates (Fig. 6c), and larger rain mixing ratio  $q_r$  (Fig. 6e) than those in MY3 (Figs. 6b,d,f, respectively). The scatter in  $D_{mr}$  is also much greater in MY3 than in MY1A. A closer look reveals that the spatial pattern of  $D_{mr}$  in MY1 follows very closely that of the  $q_r$  contours (Fig. 7a), while there is much greater variation in MY3 with the largest  $D_{mr}$  occurring near the south edge of the forward flank (Fig. 7b). This pattern agrees well with observations of high  $Z_{DR}$  (a proxy for  $D_{mr}$ ) in this region of supercells (Kumjian and Ryzhkov 2008; Romine et al. 2008). This behavior is a consequence of the absence (presence) of the size-sorting effect in 1M (3M) moment schemes that is described in

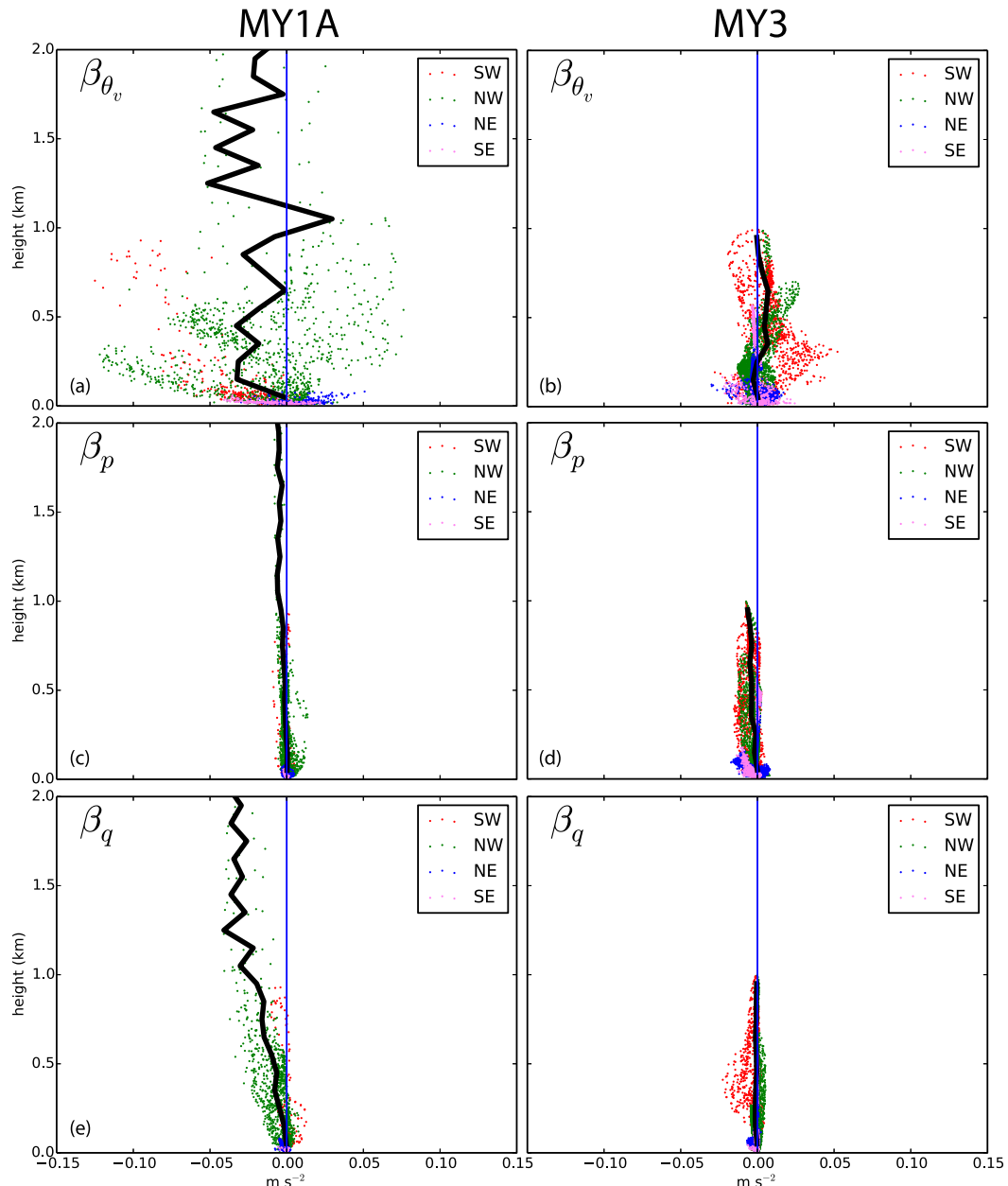


FIG. 5. Scatterplots of (a),(b) thermal  $\beta_{\theta_v}$ , (c),(d) pressure  $\beta_p$ , and (e),(f) water loading  $\beta_q$  effective buoyancy acceleration for all TLV trajectory points in the pre-TLV period vs height AGL for (left) MY1A for the 4890 s reference time and (right) MY3 for the 4380 s reference time (i.e., the same reference times as shown in Fig. 4). The thick black lines in each plot represent the 100-m binned averages. Additionally, the points are colored according to which quadrant relative to the TLV location they are located at the given time: southwest (SW), red; northwest (NW), green; northeast (NE), blue; and southeast (SE), violet.

detail in Kumjian and Ryzhkov (2012) and Dawson et al. (2014). Parcels entering the TLV from the NW and SW quadrants in both experiments tend to have the largest magnitudes of  $D_{mr}$  (green and black points in Figs. 6a,b). This is consistent with the relatively larger magnitudes of  $D_{mr}$  in the neck of the hook echo and storm core in both cases (Fig. 7) but the average value is roughly 2.5

times greater in MY3 (~2.5–3.0 mm) than in MY1A (~1.0 mm). The large amount of small-drop trajectory points at low levels in MY3 in the southeast and northeast quadrants (Fig. 6b, purple and blue points, respectively) is a consequence of the presence of low clouds in the storm inflow that are producing small raindrops via warm-rain processes. However, the rain-evaporation

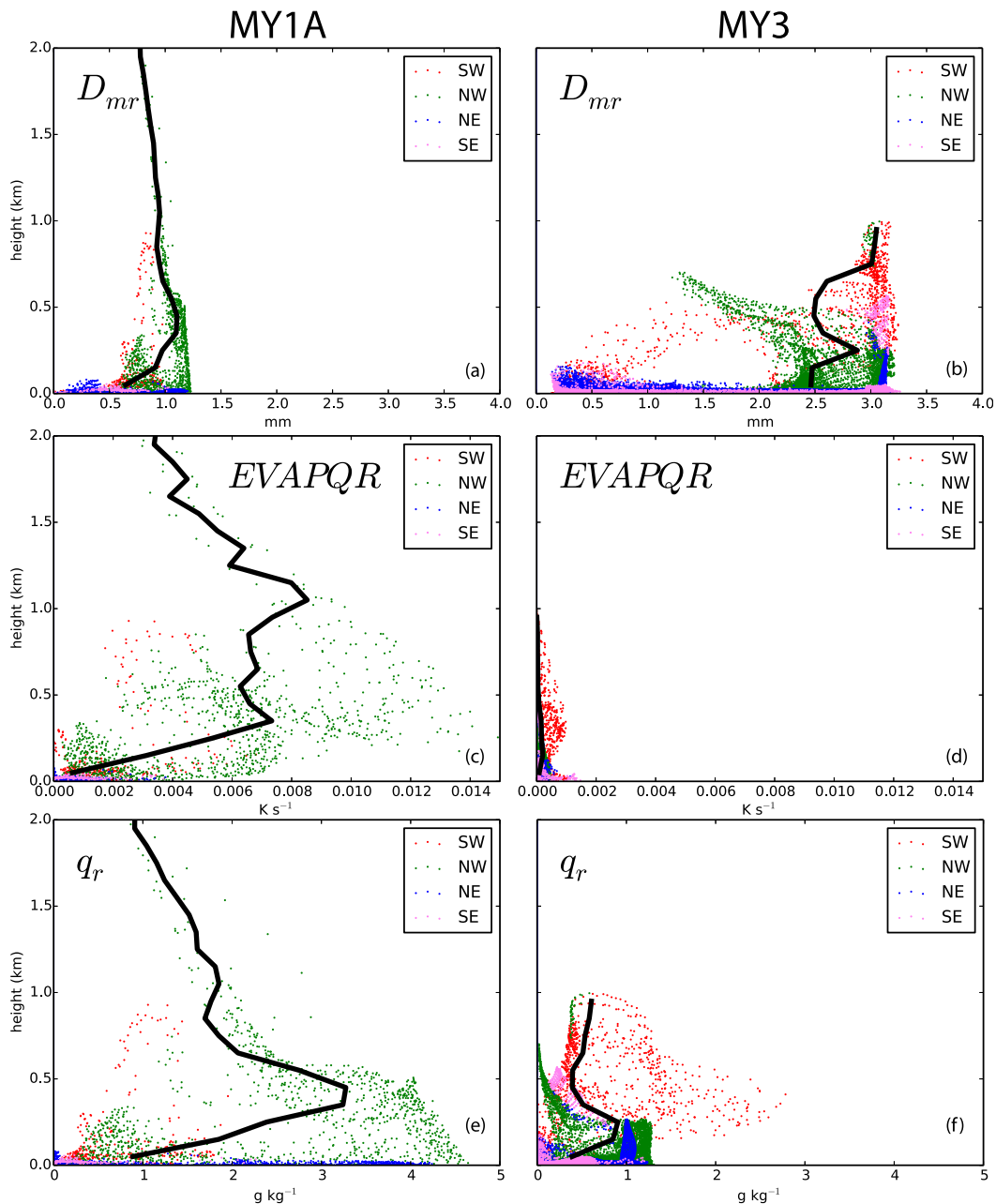


FIG. 6. As in Fig. 5 but for (a),(b) rain mean volume diameter  $D_{mr}$  (mm), (c),(d) instantaneous rain evaporative cooling rate (EVAPQR,  $K s^{-1}$ ), and (e),(f) rain mixing ratio  $q_r$  ( $g kg^{-1}$ ). Only points with nonzero  $q_r$  are shown.

rates in this region are very low owing to both the very high relative humidity in the storm inflow (not shown) and the overall small magnitudes of  $q_r$  (Fig. 6f). A similar scenario is evident when considering the impacts of melting hail (Fig. 8) except that the average hail mean volume diameter  $D_{mh}$  is greater for most heights in MY1A than in MY3 (see corresponding discussion in Part I). Most of the hail in MY1A is found in the NW quadrant (green points in Fig. 8), which

corresponds to the main body of the hook echo precipitation and overall  $q_h$  is much greater in MY1A than in MY3 (Figs. 8e,f, respectively).

More parcels experience periods of downward DVPPGA in MY3 than in MY1A (Fig. 9d versus Fig. 9c). This result indicates that the predominant mechanisms forcing descent of parcels that later enter the TLV are different between the two experiments: namely, pre-TLV downdraft parcels are

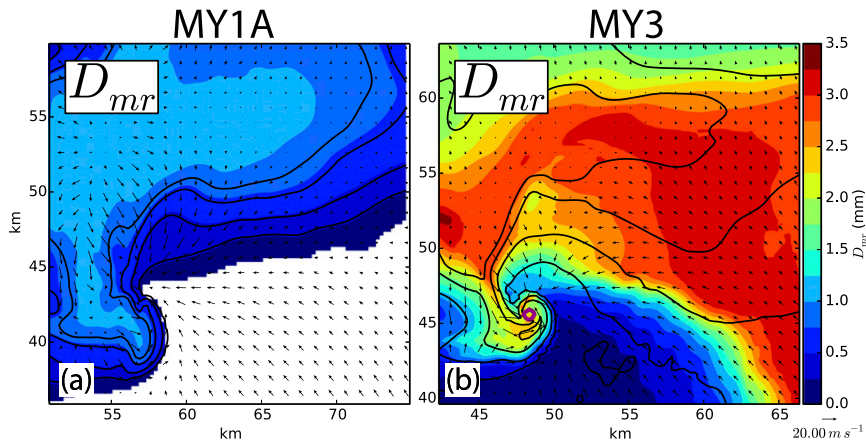


FIG. 7. Surface rain mean volume diameter  $D_{mr}$  (color shading), rainwater mixing ratio  $q_r$  (black contours; 0.01, 0.1, 0.5, 1.0, 5.0  $\text{g kg}^{-1}$  indicated), vertical vorticity  $\zeta$  (purple,  $0.1\text{-s}^{-1}$  contour shown), and ground-relative wind vectors at the first scalar point above ground ( $\sim 10$  m), plotted every 500 m in the horizontal for (a) MY1A at 4890 s and (b) MY3 at 4380 s.

predominantly buoyantly driven in MY1A (but largely cancelled by upward DVPPGA as the parcels descend toward the ground), whereas there are more dynamically driven downdraft parcels in MY3. Finally, as also seen in Figs. 4a,b, there are more parcels descending from greater altitudes ( $>1$  km) in MY1A than in MY3, and these also tend to be negatively buoyant, which is consistent with the deeper profiles of evaporation and melting in MY1A (see Part I for further discussion).

The black lines in the trajectory scatterplots (Fig. 5 and similar figures) represent the averages of the variables for each 100-m height bin. To get an idea of the temporal evolution of the TLV trajectories, we can plot these averages as a function of height and reference time. These are shown for  $\beta$  and DVPPGA in Fig. 10. From this perspective, the overall evolution of the TLV in MY1A versus MY3 is consistent with that shown for the individual “peak intensity” reference time above—namely, that the parcels entering the TLV have a history of greater negative buoyancy associated with greater latent cooling and hydrometeor mass in MY1A than in MY3, particularly for trajectory points below 1 km AGL (Fig. 10a versus Fig. 10c). Trajectories entering the TLV in MY3 that descend from aloft also tend to encounter a region of strong downward DVPPGA between about 500 and 1500 km AGL that is more prevalent than in MY1A. The TLV in MY3 exhibits some time periods where some parcels descend from a greater height than in MY1A, in contrast to the peak intensity time discussed in the previous section. However, the fraction of trajectories (for a given reference time) beginning above 1 km AGL in the pre-TLV period is much smaller in

MY3 relative to MY1A for most of the evolution of the TLV (Fig. 11).

### c. Trajectory analysis for the intra-TLV period

We explore the behavior of parcels after entering the TLV in a manner similar to the pre-TLV trajectory analysis by examining scatterplots and time–height plots of height-binned trajectory points during the intra-TLV period. In Figs. 12–14, the trajectory points are colored by the magnitude of their instantaneous vertical velocity  $w$ , and the size of the points is related to the negative magnitude of their pressure perturbation  $p'$ . The components of  $\beta$  exhibit dramatic differences from their pre-TLV behavior (Fig. 12). This is due to the large dynamically induced pressure drop within the TLV itself (Fig. 13), associated with the centrifugal force. This negative  $p'$  contributes to substantial positive  $\beta_p$  (Figs. 12b,c), particularly in MY3, which has an average pressure drop approximately twice that of MY1A (cf. Figs. 13a,b), particularly below 1 km AGL. Indeed,  $\beta_p$  is by far the dominant positive term in the buoyancy forcing in the low levels for both experiments: approximately 75% of the total positive  $\beta$  forcing in MY3 below 2 km AGL comes from the effective pressure buoyancy  $\beta_p$  (cf. Figs. 12b,d). In MY1A, this contribution is nearly 100% (cf. Figs. 12a,c). However, the overall magnitude of  $\beta_p$  is much lower than in MY3 (cf. Figs. 12c,d), and MY1A exhibits primarily negative  $\beta_{\theta_v}$  below 1 km AGL (Fig. 12a).

In contrast, parcels in MY3 exhibit rapidly increasing  $\beta_{\theta_v}$  with height up to nearly 5 km AGL (Fig. 12b), which represents the farthest parcels are able to ascend in the

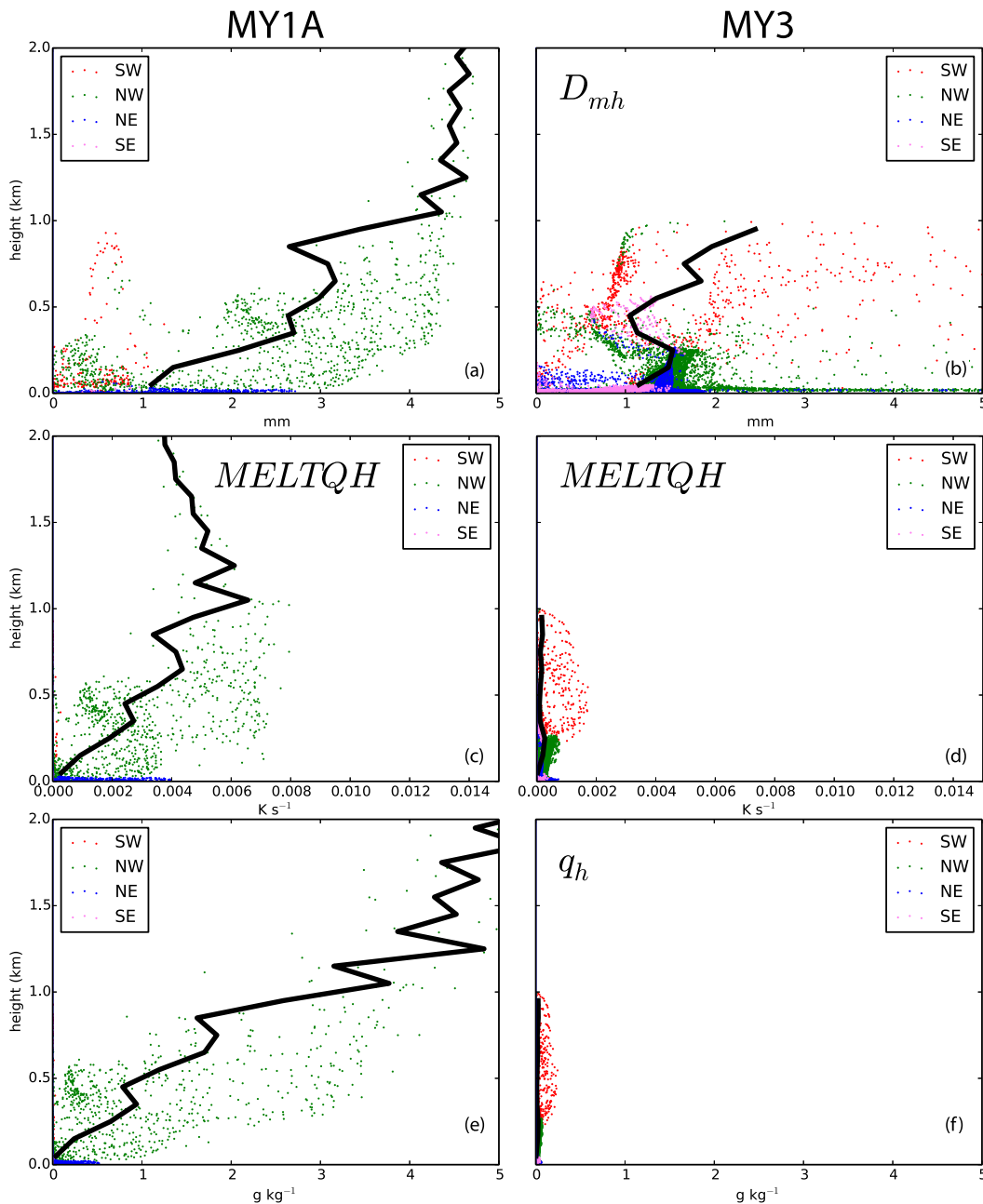


FIG. 8. As in Fig. 6, but for hail.

intra-TLV period (maximum of 5 min). This increase is ultimately due to latent heating from condensation as parcels quickly reach their LFC and is consistent with the modeling study of Naylor and Gilmore (2014) and the observational study of Davies (2004), who found a correlation with relatively low LFCs and tornadic activity. By extension, this result is also consistent with the findings of Rasmussen and Blanchard (1998), Thompson et al. (2003), and Craven and Brooks (2004) that supercell environments with relatively low LCLs are more

likely to produce strong tornadoes.<sup>3</sup> These studies suggested that lower evaporation potential in the subcloud layer and correspondingly warmer and more buoyant storm outflow are responsible for this correlation. Our results suggest that, at least for environments with relatively weak CIN, a further explanation may be found in

<sup>3</sup> Since a relatively low LFC implies a relatively low LCL, but not vice versa. See discussion in Davies (2004).

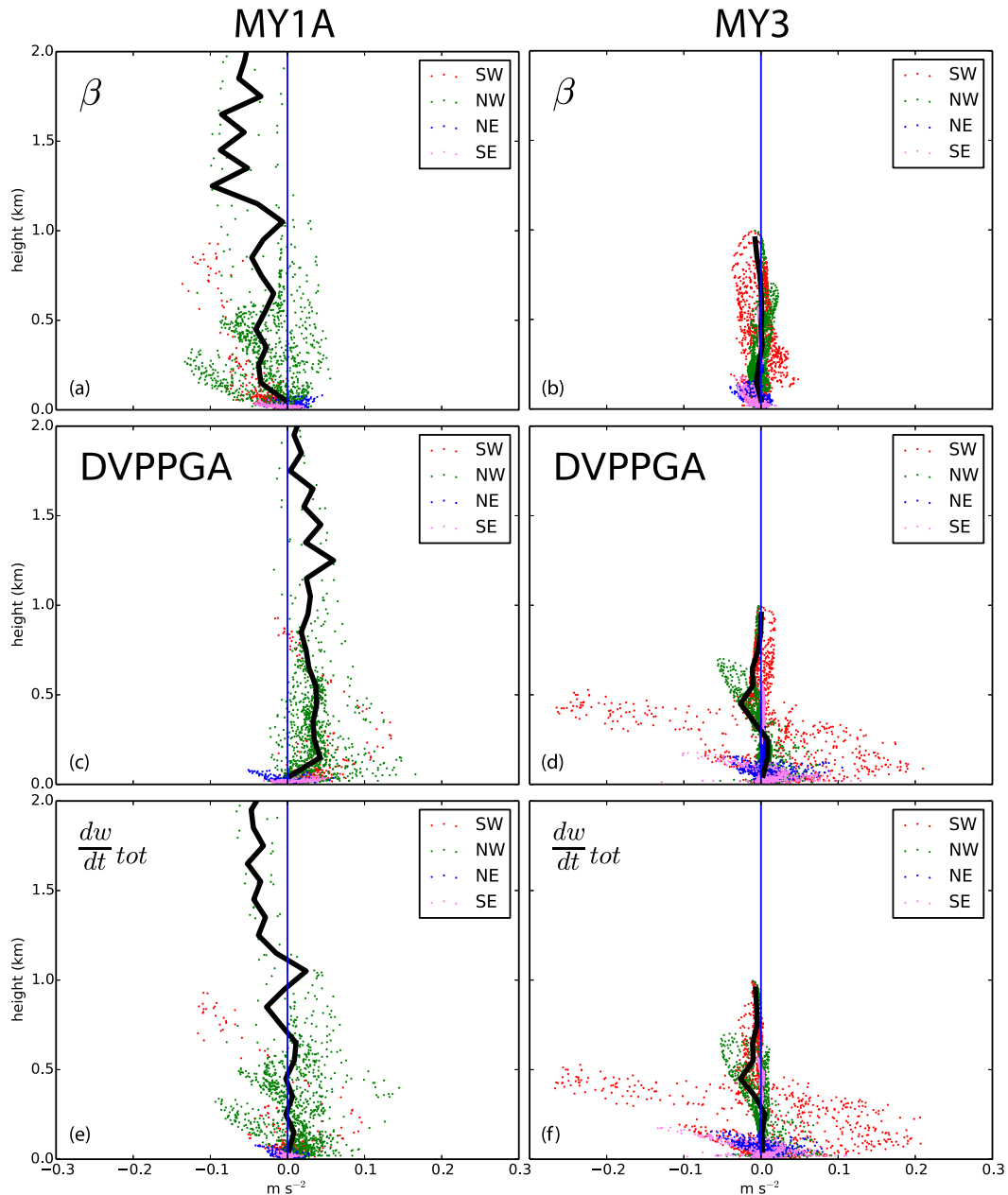


FIG. 9. As in Fig. 5, but for (a),(b) total effective buoyancy acceleration  $\beta$ , (c),(d) dynamic vertical perturbation pressure gradient acceleration (DVPPGA), and (e),(f) total (Lagrangian) vertical acceleration (i.e., the sum of  $\beta$  and DVPPGA).

the additional boost to the low-level updraft by the earlier onset of positive  $\beta_{\theta_v}$ . Davies (2004, 2006) made similar arguments. Parcels accelerated upward by dynamic and pressure buoyancy effects in the TLV are more likely to become positively thermally buoyant before succumbing to the downward DVPPGA associated with the vertical decrease in rotation of the tornado itself (i.e., the so-called vortex-valve effect; Davies-Jones 1986). In MY1A, the weaker nature of the TLV is evident by the fact that parcels are unable to

ascend as far as in MY3, and the total  $\beta$  is substantially smaller than in MY3 (Figs. 14a,b).

In both MY1A and MY3, upward DVPPGA (Figs. 14c,d) dominates in the lowest few hundred meters, associated with the strong near-surface convergence into the TLV (not shown), but is particularly intense in MY3. Above this level, a large amount of scatter is evident, which is due to the tilt of the TLV (not shown): parcels alternately experience downward and upward DVPPGA as they spiral from one side of the tilted vortex to the other.

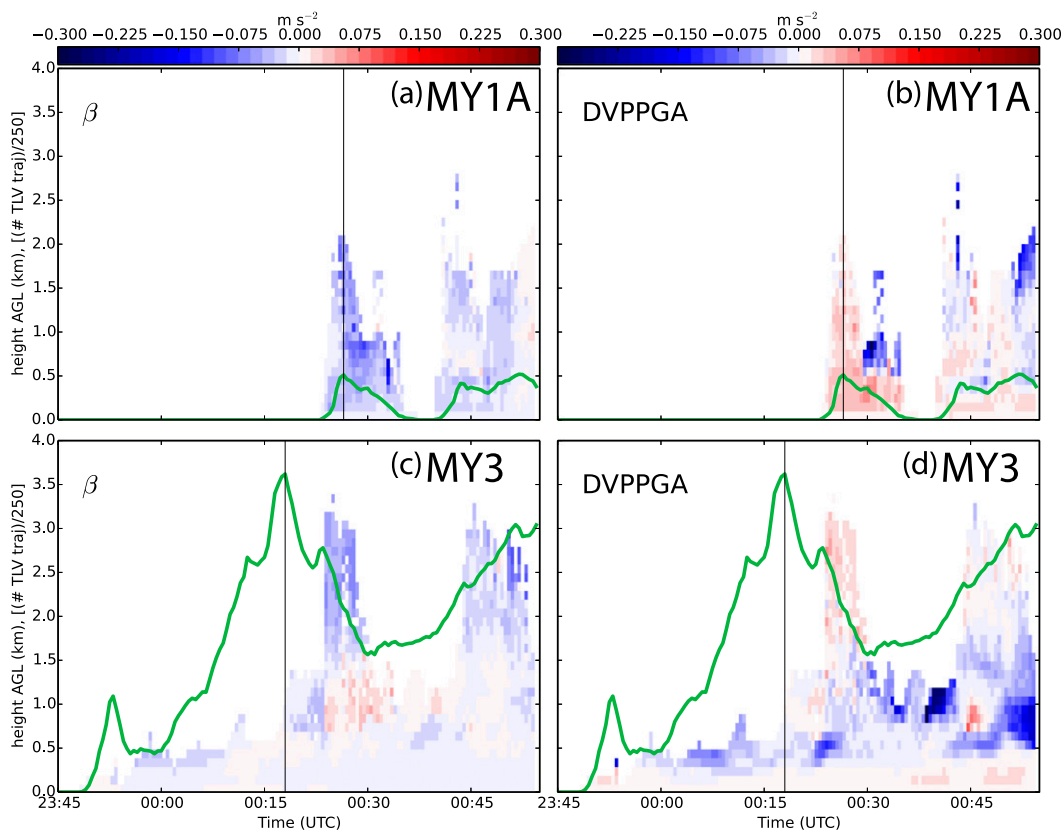


FIG. 10. Time–height plots of average (a),(c)  $\beta$  and (b),(d) DVPPGA for (top) MY1A and (bottom) MY3, for trajectories in the pre-TLV periods. Also plotted in each panel are the total numbers of trajectories (out of a total of 2401 for each reference time; cf. Fig. 3) scaled by dividing by a factor of 250 (thick green curve), and the reference time of peak intensity for each case (vertical black line), corresponding to those in Fig. 3.

Additionally, some of these parcels are actually descending within the axial downdraft of the TLV (blue shading for  $w < 0$  in Figs. 12–14). After averaging out these oscillations, DVPPGA is generally negative over most of the depth of the TLV in both MY1A and MY3 (black lines in Figs. 14c,d). In MY3, however, the negative DVPPGA below 1 km AGL is compensated for by the large positive  $\beta$  (dominated by  $\beta_p$ ), such that the overall vertical acceleration through  $\sim 2$  km AGL is positive (Fig. 14e). Parcels tend to reach their maximum  $w$  of  $40 \text{ m s}^{-1}$  or greater around 2 km AGL (dark red circles in Fig. 14, right column) with generally decreasing positive  $w$  above that level. In contrast, in MY1A, the magnitude of total vertical acceleration is much smaller than in MY3 through 2 km and small but negative above (Fig. 14f). Accordingly, maximum positive  $w$  experienced by parcels is lower, around  $20\text{--}30 \text{ m s}^{-1}$  (red circles, Fig. 14, left column).

#### 4. Physical interpretation of pressure buoyancy

The finding that effective pressure buoyancy  $\beta_p$  (and by extension, the “traditional” pressure buoyancy  $B_p$ )

plays a large role in the vertical momentum budget of the TLVs in this study is supported by the earlier axisymmetric study of Leslie and Smith (1978). We now turn to a discussion of the physical interpretation of this term.

First, we note that  $\beta_p$  tends to be large and positive in regions where  $p'$  is large and negative (cf. Fig. 12d and Fig. 13d). To illustrate this more explicitly, Fig. 15a shows a time–height profile of  $p'$  in the core of the long-lived TLV in MY3, while Fig. 15b shows the corresponding  $\beta_p$  (fields are horizontally averaged over the core of the vortex for points with  $\zeta > 0.05 \text{ s}^{-1}$ ). In general the most intense pressure drop in the core occurs near the surface for most of the lifetime of the TLV, decreasing in intensity with increasing height;  $\beta_p$  exhibits a qualitatively similar pattern, except near the surface owing to the lower boundary condition (see section 2a). On the other hand, the decrease in the magnitude of (negative)  $p'$  with height is reflected in a general negative (downward directed) DVPPGA through much of the depth of the TLV (Fig. 15c; except near the surface where strong convergence leads to a

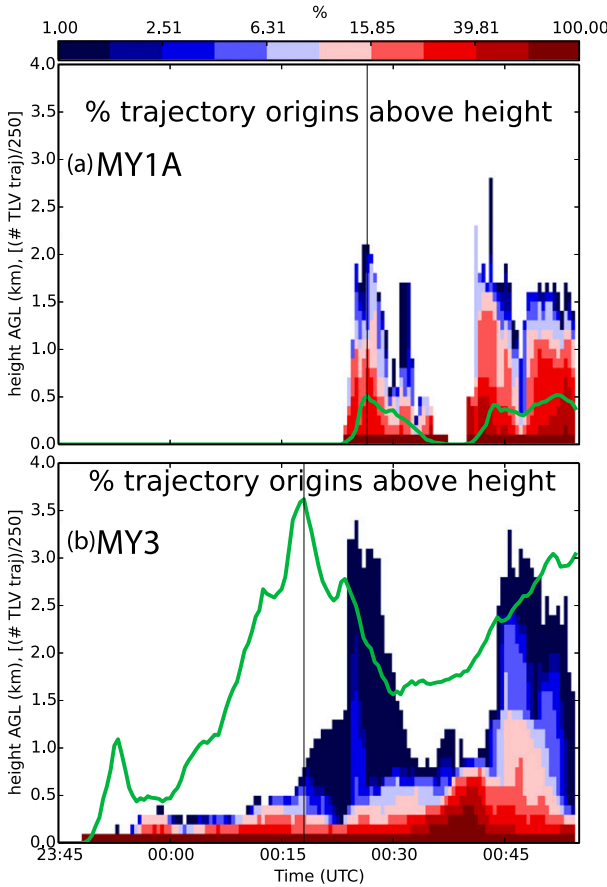


FIG. 11. Percentage of pre-TLV trajectory origin points above a given height vs reference time for (a) MY1A and (b) MY3. Green curves and vertical black lines are as in Fig. 10.

strong upward-directed DVPPGA). The sum of  $\beta_p$  and DVPPGA is shown in Fig. 15d, and it can be seen that the large positive  $\beta_p$  more than compensates for the negative DVPPGA in this case through much of the depth of the TLV aloft. The key point is that  $\beta_p$  in the core of a tornado or TLV ultimately depends on horizontal variations of the pressure field (and qualitatively on the magnitude of the pressure drop in the core), while the DVPPGA instead depends on its vertical gradient (more precisely, the vertical gradient of the dynamic part  $p'_d$  only, but in tornadoes  $p'_d$  is a large fraction of total  $p'$ ). Since the relative contributions of DVPPGA and  $\beta_p$  in the core of the tornado depend on different aspects of the TLV pressure distribution, they conceivably may vary independently. To illustrate with a simple example, consider two idealized tornadoes, each with different overall magnitudes of the core pressure drop, but with the same downward-directed DVPPGA. (Such a scenario may be approximated in nature if a tornado intensifies relatively uniformly with height. Often, of course, the DVPPGA will not remain constant

as a tornado intensifies, but will instead also increase in magnitude as the pressure drops more quickly in the lower levels of the vortex; the main point here is that this is not physically inevitable.) We illustrate this scenario schematically in Fig. 16. We see that the greater the overall magnitude of the pressure drop in the TLV for a given negative DVPPGA, the more the resulting larger positive  $\beta_p$  compensates for the negative DVPPGA (cf. the “strong” and “weak” cases in Fig. 16a and Fig. 16b, respectively).

The fact that  $\beta_p$  (or  $B_p$ ) is related to the total pressure perturbation  $p' = p'_d + p'_b$  indicates that it can be interpreted as including a dynamic feedback to the static forcing. This is particularly true in tornadoes, where intense circulation dynamically supports a large fraction of the core pressure drop. When (3) is written in terms of the Exner function  $\pi$  instead of physical pressure  $p$  and potential temperature  $\theta$  in place of density  $\rho$  (hereafter the “ $\pi - \theta$ ” and “ $p - \rho$ ” forms, respectively), the pressure buoyancy  $B_p$  no longer explicitly appears in the vertical momentum equation [see, e.g., Houze (1993)], being absorbed by the VPPGF term (Markowski and Richardson 2010). Indeed, this is often taken as an advantage of the  $\pi - \theta$  form, as it simplifies the mathematical presentation. Moreover, the combination of  $B_p$  and the VPPGF into one term in the  $\pi - \theta$  form would appear to cohere with our physical interpretation of  $B_p$ . Yet, we first made this interpretation based on an analysis done using the  $p - \rho$  form, and the consequence of this gain in mathematical elegance is that the foregoing physically motivated decomposition into dynamic and static components is at least partially obscured. For these reasons, we argue that a deeper physical understanding is gained when the vertical momentum equation is written in the  $p - \rho$  form.

Since the large contribution to upward buoyancy accelerations from the low-pressure perturbation within the TLV depends on the existence of the vortex in the first place, the pressure buoyancy cannot be the primary vertical forcing for tornadogenesis. It is better to view  $\beta_p$  as locally modulating the intensity of the vortex by opposing the downward DVPPGA in the core (the aforementioned “vortex-valve effect”) provided another mechanism is in place to otherwise sustain the vortex (namely the overlying buoyant updraft and mesocyclone). We speculate that the primary role of  $\beta_p$  may be to aid in physically “connecting” the vortex with this overlying “support structure.” We further note that we are not suggesting that the “pressure buoyancy effect” would provide an unending positive feedback loop (as might be implied by the fact that its magnitude increases with the increasing intensity of the tornado). As

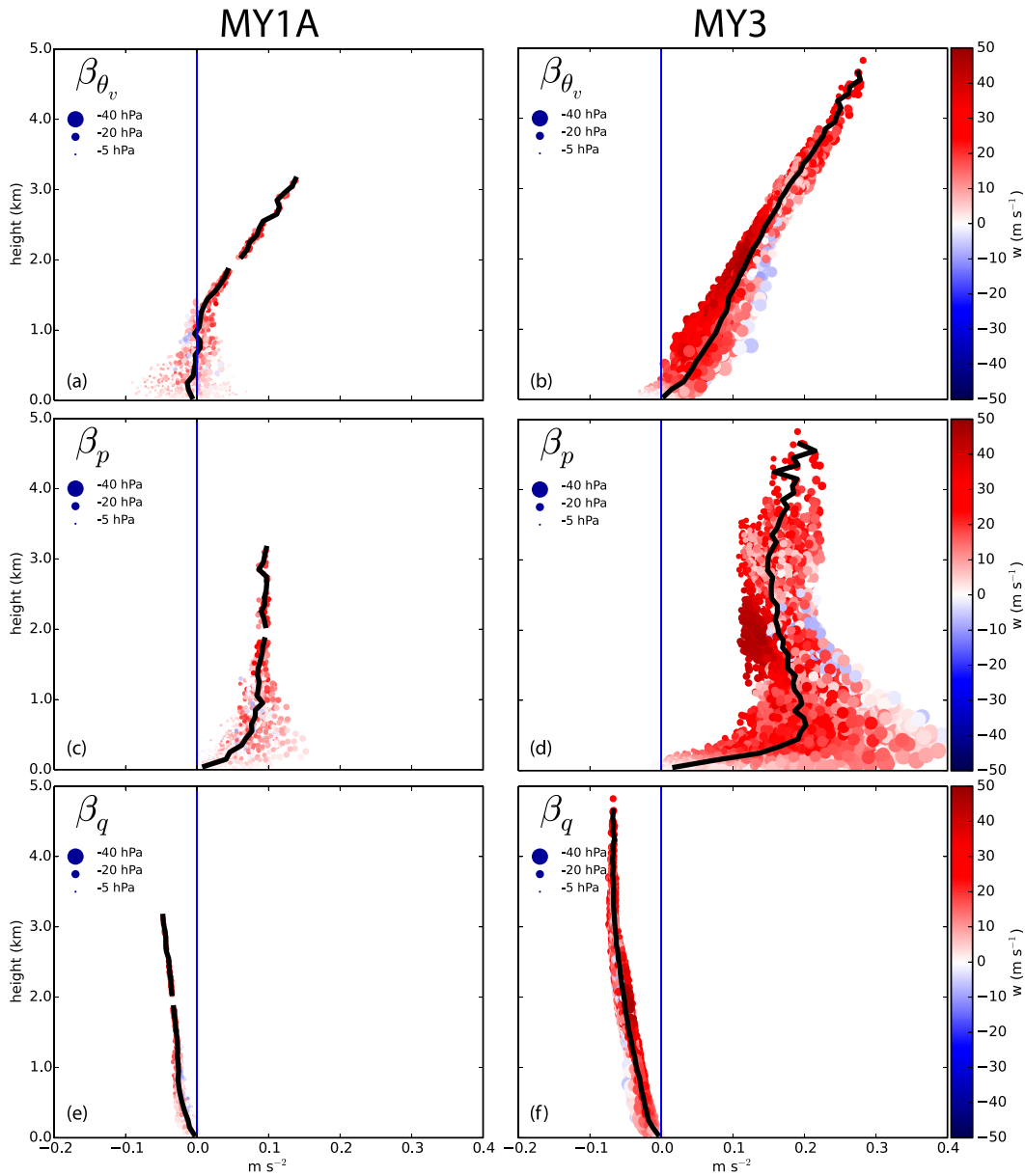


FIG. 12. As in Fig. 5, but for all TLV trajectory points in the intra-TLV period. Additionally, the points are now colored according to the instantaneous magnitude of vertical velocity  $w$  ( $\text{m s}^{-1}$ ) and the sizes represent the magnitude of the instantaneous pressure perturbation  $p'$  (hPa; legend in upper left of each panel).

discussed in Eskridge et al. (1979), this can clearly be ruled out on energy budget considerations.

Whether there is any additional role of  $\beta_p$  (or  $B_p$ ) in terms of fundamental vortex dynamics remains unclear and requires further investigation. Many previous numerical studies of tornado dynamics have effectively neglected  $B_p$  by imposing the Boussinesq approximation or even the more restrictive assumption of constant density on the governing equations. However, Xia et al. (2003) showed that much of the effect of compressibility

on the pressure field of a simulated tornado could be recovered even in an incompressible, constant density model via a diagnostic “isentropic transform” procedure. In the new, “reinterpreted” pressure field, the effect of  $B_p$  is now implicitly included (D. Lewellen 2015, personal communication) for a given velocity structure. Importantly, these aforementioned idealized studies were largely concerned with elucidating the basic dynamics of tornadoes, rather than attempting to simulate them within the context of a realistic parent

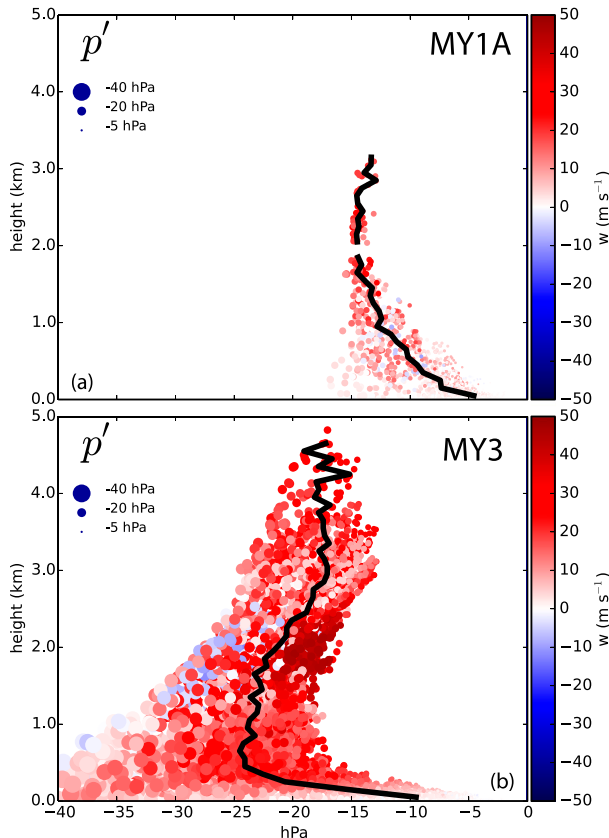


FIG. 13. As in Fig. 12, but for perturbation pressure  $p'$  (hPa) for (a) MY1A and (b) MY3.

thunderstorm. As we have shown, in this more complex scenario, neglecting this term clearly will lead to large errors.

## 5. Summary and conclusions

In Part II of this study, we investigated the impact of 1M versus 3M bulk microphysics on simulated tornadic activity (i.e., tornado-like vortices or TLVs) in the high-resolution (250-m grid spacing) simulations of an F5 tornado discussed in Part I. Specifically, we chose for detailed analysis two of the 250-m simulations representing the high evaporation–strong cold pool (MY1A) and the low evaporation–weak cold pool (MY3) extremes, obtained using a 1M and 3M version of a multimoment microphysics scheme. Our main goals were to 1) investigate the differences in the microphysical and thermodynamic properties of the air flowing into the TLVs using a trajectory analysis and 2) assess the relative importance of buoyant versus dynamic vertical momentum forcing both before and after the air entered the TLVs. Systematic differences between buoyant versus dynamic forcing for

vertical motion were seen in the TLVs of the two experiments, with MY3 producing an intense, long-lasting TLV with behavior more similar to the observed tornado. The main findings of this study are as follows:

- 1) A trajectory analysis revealed that the air flowing into the TLV in MY3 was dominated by largely unmodified inflow air. The existence of a large number of inflow trajectories in our study contrasts with the results of Dahl et al. (2012), who found that trajectories entering their simulated TLV were almost exclusively derived from the storm-generated outflow. Also, trajectories descending through the rear-flank downdraft experienced relatively minor amounts of rain evaporation and hail melting prior to entering the tornado.
- 2) In contrast, a greater percentage of TLV trajectories in MY1A descended through a greater depth. They also tended to experience much more evaporative cooling from rain and melting from hail as well as more hydrometeor loading. The differences in evaporative cooling were tied to the larger mean rain diameters [ $O(3\text{ mm})$ ] in MY3 as compared with MY1A [ $O(1\text{ mm})$ ] as well as greater amounts of rain overall. Cooling by melting of hail was greater in MY1A owing primarily to the much larger amounts of hail in the low levels when compared to MY3.
- 3) With the greater latent cooling and hydrometeor loading in MY1A, parcels converging into the TLV were typically negatively thermally buoyant by the time they reached the TLV. In agreement with previous observational (Markowski 2002; Markowski et al. 2002; Lee et al. 2012) and modeling studies (Leslie and Smith 1978; Markowski et al. 2003; Parker 2012; Markowski and Richardson 2014), the more negatively buoyant air contributed to a weaker TLV.
- 4) In both MY1A and MY3, the vertical accelerations were dominated by upward dynamic VPPGA in the lowest levels (in the lowest few hundred m AGL). In MY3, the thermal buoyancy of the air flowing into the intense and long-lasting TLV was on average neutral or slightly negative, while it was more negative in the weaker, short-lived TLV in MY1A. For most of the life cycle of the TLV in both MY3 and MY1A, positive pressure buoyancy dominated all other terms in the buoyancy but was substantially weaker in MY1A. This finding corroborates the earlier highly idealized study of Leslie and Smith (1978) and confirms that this term plays an important role in the vertical momentum budget of tornadoes. Many previous analyses of tornado

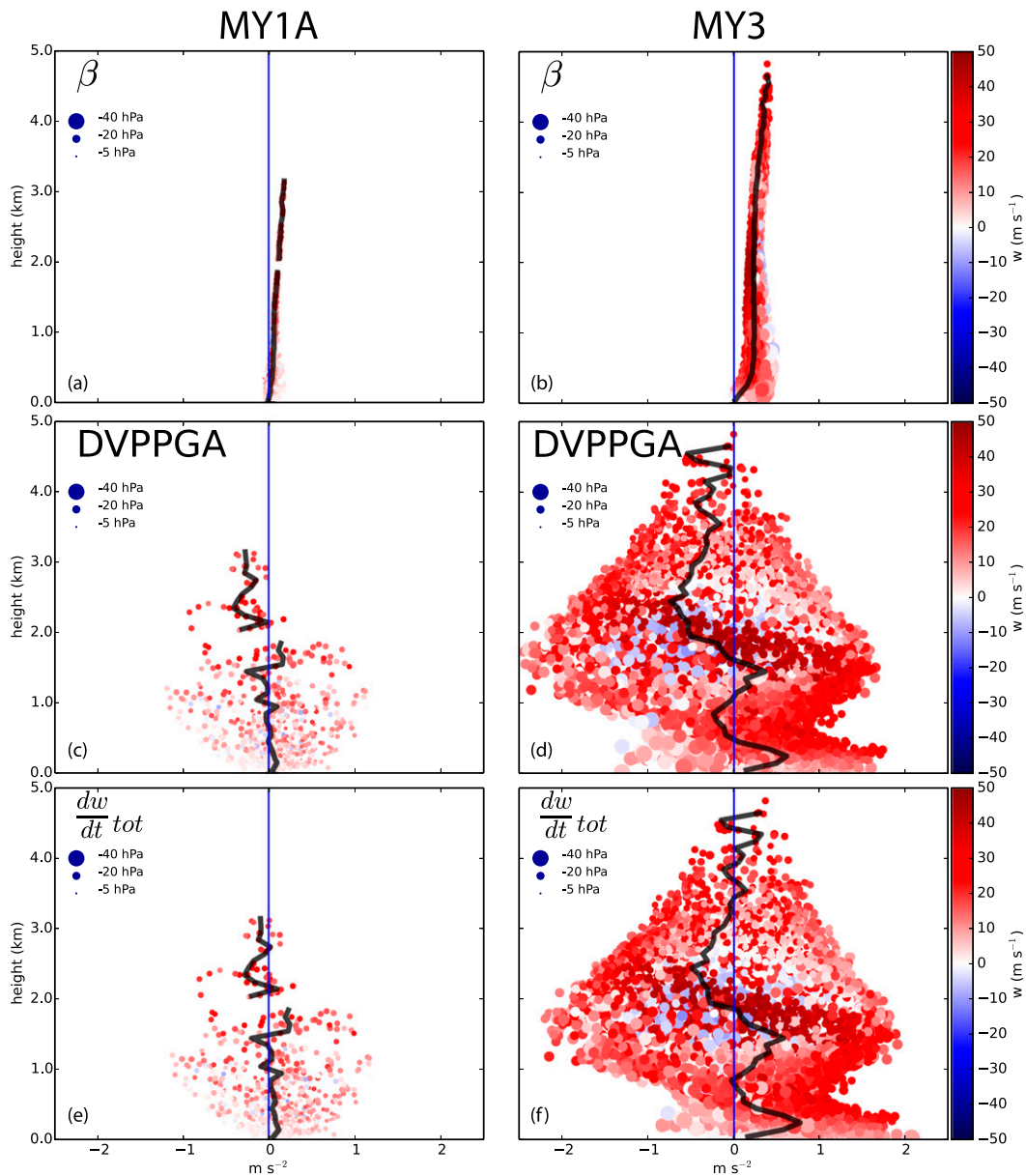


FIG. 14. As in Fig. 9, but for TLV trajectory points in the intra-TLV period (color and size of points as in Fig. 11). Note the different scale on the  $x$  axis from that in Fig. 9.

dynamics have implicitly included the pressure buoyancy effect but have not clearly explained its nature. We provided a physical interpretation of the pressure buoyancy in this context as a dynamic feedback to the static part of the nonhydrostatic vertical pressure gradient acceleration. This term mitigated or in some cases overwhelmed the downward dynamic VPPGA within the TLV core in our simulations.

Above about 1 km AGL within the TLV in both experiments, thermal buoyancy due to latent heat release

in the storm updraft quickly becomes an important term contributing to vertical acceleration of parcels within (stretching of) the vortex, while the dynamic VPPGA was typically downward at this level (owing to the decrease in rotational intensity, and thus the associated pressure drop, with height).

The above findings indicate that the thermodynamic characteristics of the TLV inflow have a strong and direct impact on the intensity of the TLV via their impacts on the vertical momentum budget. These characteristics, in turn, are strongly modulated by the microphysics

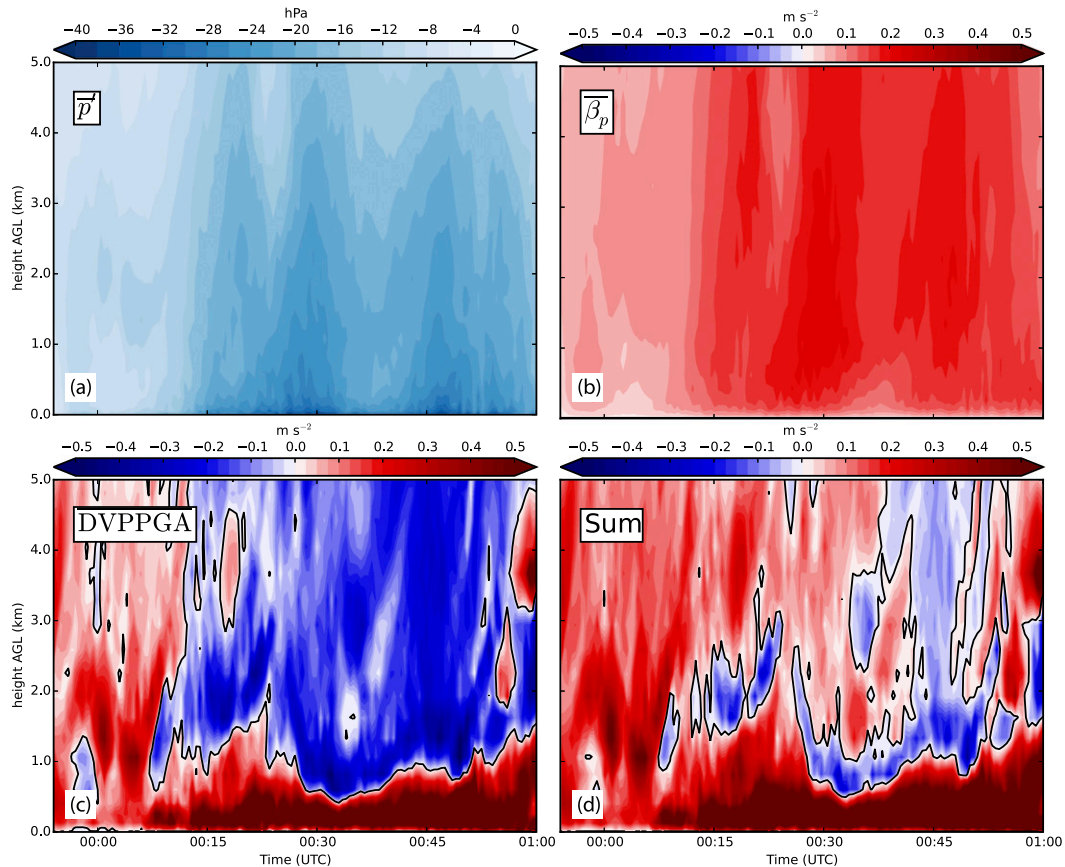


FIG. 15. Time–height plots following the long-lived TLV in MY3 for (a) pressure perturbation  $p'$ , (b) effective pressure buoyancy  $\beta_p$ , (c) dynamic vertical perturbation pressure gradient acceleration (DVPPGA), and (d) the sum of  $\beta_p$  and DVPPGA. Each field is horizontally averaged over grid points with vertical vorticity  $\zeta > 0.05 \text{ s}^{-1}$  within the TLV.

scheme via its treatment of latent cooling from evaporation and melting of hydrometeors. In our study, a 3M scheme resulted in a TLV simulation with many characteristics—notably intensity, duration, and pathlength—that were very similar to the observed 3 May 1999 Oklahoma City F5 tornado. The 1M scheme, in contrast, resulted in only weak and short-lived TLVs. We found other interesting differences in regard to surface thermal and wind boundaries: the 1M experiment contained what appeared to be a left-flank convergence boundary (LFCB; Beck and Weiss 2013) in addition to the traditional rear-flank gust front (RFGF), while the former appeared weaker or absent in the 3M experiment. Further study of these differences is warranted and will be considered in future work. Finally, we reiterate that we have not addressed the tornadogenesis problem itself in this study, but future work may examine the importance of baroclinic sources of vorticity for tornadogenesis and maintenance, especially in light of the very weak low-level thermal gradients present in the 3M experiment, which

also contained the most intense and longest-lived TLV.

In considering the potential broader impacts of this study, we submit these results as a strong argument for continued investigation into the utility of sophisticated multimoment microphysics for improvement of storm and tornado simulation and prediction—one of the main goals of the emerging warn-on-forecast paradigm (Stensrud et al. 2009, 2013).

*Acknowledgments.* This study was primarily supported by NSF AGS-0802888 and NSF AGS-1137702. The second author was also supported by NSF Grants AGS-0941491, AGS-1046171, and AGS-1261776. Computations were carried out at the Oklahoma Supercomputing Center for Education and Research (OSCER), and at the Texas Advanced Computing Center (TACC). The authors thank two anonymous reviewers and Dr. Matthew Parker for their very helpful comments that substantially strengthened the paper. The authors would also like to thank Drs. Lou Wicker,

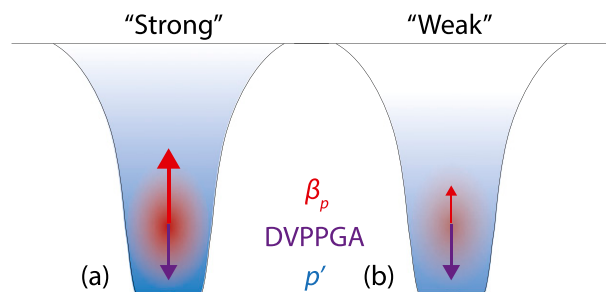


FIG. 16. Schematic of the instantaneous vertical momentum budget in the low levels of the core of a relatively (a) strong and (b) weak tornado, both with identical downward DVPPGA. Blue-to-white shading represents the overall pressure drop (negative  $p'$ ) in the core that decreases in magnitude with height, red shading indicates the region of greatest upward effective pressure buoyancy  $\beta_p$ , and red and violet arrows respectively indicate the opposing upward  $\beta_p$  and downward DVPPGA. Depending on the overall magnitude of the pressure drop, the sum of these accelerations will be upward or downward at a given level in the core.

Ted Mansell, Johannes Dahl, Dave Lewellen, Jeff Snyder, Paul Markowski, Yvette Richardson, Corey Potvin, Patrick Skinner, and Robin Tanamachi for many helpful discussions.

#### REFERENCES

- Adams, J. C., 1989: MUDPACK: Multigrid portable FORTRAN software for the efficient solution of linear elliptic partial differential equations. *Appl. Math. Comput.*, **34**, 113–146, doi:10.1016/0096-3003(89)90010-6.
- , and P. Smolarkiewicz, 2001: Modified multigrid for 3D elliptic equations with cross-derivatives. *Appl. Math. Comput.*, **121**, 301–312, doi:10.1016/S0096-3003(00)00004-7.
- Beck, J., and C. Weiss, 2013: An assessment of low-level baroclinity and vorticity within a simulated supercell. *Mon. Wea. Rev.*, **141**, 649–669, doi:10.1175/MWR-D-11-00115.1.
- Craven, J. P., and H. Brooks, 2004: Baseline climatology of sounding derived parameters associated with deep moist convection. *Natl. Wea. Dig.*, **28**, 13–24.
- Dahl, J. M. L., M. D. Parker, and L. J. Wicker, 2012: Uncertainties in trajectory calculations within near-surface mesocyclones of simulated supercells. *Mon. Wea. Rev.*, **140**, 2959–2966, doi:10.1175/MWR-D-12-00131.1.
- Das, P., 1979: A non-Archimedean approach to the equations of convection dynamics. *J. Atmos. Sci.*, **36**, 2183–2190, doi:10.1175/1520-0469(1979)036<2183:ANAATT>2.0.CO;2.
- Davies, J. M., 2004: Estimations of CIN and LFC associated with tornadic and nontornadic supercells. *Wea. Forecasting*, **19**, 714–726, doi:10.1175/1520-0434(2004)019<0714:EOCALA>2.0.CO;2.
- , 2006: Tornadoes with cold core 500-mb lows. *Wea. Forecasting*, **21**, 1051–1062, doi:10.1175/WAF967.1.
- Davies-Jones, R. P., 1986: Tornado dynamics. *Thunderstorm Morphology and Dynamics*, E. Kessler, Ed., University of Oklahoma Press, 197–236.
- , 2003: An expression for effective buoyancy in surroundings with horizontal density gradients. *J. Atmos. Sci.*, **60**, 2922–2925, doi:10.1175/1520-0469(2003)060<2922:AEFEFI>2.0.CO;2.
- Dawson, D. T., E. R. Mansell, Y. Jung, L. J. Wicker, M. R. Kumjian, and M. Xue, 2014: Low-level ZDR signatures in supercell forward flanks: the role of size sorting and melting of hail. *J. Atmos. Sci.*, **71**, 276–299, doi:10.1175/JAS-D-13-0118.1.
- , M. Xue, J. A. Milbrandt, and A. Shapiro, 2015: Sensitivity of real-data simulations of the 3 May 1999 Oklahoma City tornadic supercell and associated tornadoes to multi-moment microphysics. Part I: Storm- and tornado-scale numerical forecasts. *Mon. Wea. Rev.*, **143**, 2241–2265, doi:10.1175/MWR-D-14-00279.1.
- Doswell, C. A., and P. M. Markowski, 2004: Is buoyancy a relative quantity? *Mon. Wea. Rev.*, **132**, 853–863, doi:10.1175/1520-0493(2004)132<0853:IBARQ>2.0.CO;2.
- Emanuel, K. A., 1994: *Atmospheric Convection*. Oxford University Press, 580 pp.
- Eskridge, R. E., P. Das, R. K. Smith, and L. M. Leslie, 1979: Comment on the paper entitled ‘Tornadogenesis’ by R. K. Smith and L. M. Leslie (*Q.J.*, 104, 189–199). *Quart. J. Roy. Meteor. Soc.*, **105**, 310–313, doi:10.1002/qj.49710544322.
- Gilmore, M. S., J. M. Straka, and E. N. Rasmussen, 2004: Precipitation uncertainty due to variations in precipitation particle parameters within a simple microphysics scheme. *Mon. Wea. Rev.*, **132**, 2610–2627, doi:10.1175/MWR2810.1.
- Houze, R. A., Jr., 1993: *Cloud Dynamics*. Academic Press, 573 pp.
- Jeevanjee, N., and D. M. Romps, 2015: Effective buoyancy, inertial pressure, and the mechanical generation of boundary-layer mass flux by cold pools. *J. Atmos. Sci.*, **72**, 3199–3213, doi:10.1175/JAS-D-14-0349.1.
- Kumjian, M. R., and A. V. Ryzhkov, 2008: Polarimetric signatures in supercell thunderstorms. *J. Appl. Meteor. Climatol.*, **47**, 1940–1961, doi:10.1175/2007JAMC1874.1.
- , and —, 2012: The impact of size sorting on the polarimetric radar variables. *J. Atmos. Sci.*, **69**, 2042–2060, doi:10.1175/JAS-D-11-0125.1.
- Lee, B. D., C. A. Finley, and C. D. Karstens, 2012: The Bowdle, South Dakota, cyclic tornadic supercell of 22 May 2010: Surface analysis of rear-flank downdraft evolution and multiple internal surges. *Mon. Wea. Rev.*, **140**, 3419–3441, doi:10.1175/MWR-D-11-00351.1.
- Leslie, L. M., and R. K. Smith, 1978: The effect of vertical stability on tornadogenesis. *J. Atmos. Sci.*, **35**, 1281–1288, doi:10.1175/1520-0469(1978)035<1281:TEOVSO>2.0.CO;2.
- Ludlam, F. H., 1963: Severe local storms: A review. *Severe Local Storms, Meteor. Monogr.*, No. 27, Amer. Meteor. Soc., 1–30.
- Markowski, P. M., 2002: Mobile mesonet observations on 3 May 1999. *Wea. Forecasting*, **17**, 430–444, doi:10.1175/1520-0434(2002)017<0430:MMOOM>2.0.CO;2.
- , and Y. Richardson, 2010: *Mesoscale Meteorology in Mid-latitudes*. John Wiley and Sons, 407 pp.
- , and Y. P. Richardson, 2014: The influence of environmental low-level shear and cold pools on tornadogenesis: Insights from idealized simulations. *J. Atmos. Sci.*, **71**, 243–275, doi:10.1175/JAS-D-13-0159.1.
- , J. M. Straka, and E. N. Rasmussen, 2002: Direct surface thermodynamic observations within the rear-flank downdrafts of nontornadic and tornadic supercells. *Mon. Wea. Rev.*, **130**, 1692–1721, doi:10.1175/1520-0493(2002)130<1692:DSTOWT>2.0.CO;2.
- , —, and —, 2003: Tornadogenesis resulting from the transport of circulation by a downdraft: Idealized numerical simulations. *J. Atmos. Sci.*, **60**, 795–823, doi:10.1175/1520-0469(2003)060<0795:TRFTTO>2.0.CO;2.

- Marshall, J. S., and W. M. Palmer, 1948: The distribution of raindrops with size. *J. Meteor.*, **5**, 165–166, doi:10.1175/1520-0469(1948)005<0165:TDORWS>2.0.CO;2.
- Milbrandt, J. A., and M. K. Yau, 2005: A multi-moment bulk microphysics parameterization. Part II: A proposed three-moment closure and scheme description. *J. Atmos. Sci.*, **62**, 3065–3081, doi:10.1175/JAS3535.1.
- Naylor, J., and M. S. Gilmore, 2014: Vorticity evolution leading to tornadogenesis and tornadogenesis failure in simulated supercells. *J. Atmos. Sci.*, **71**, 1201–1217, doi:10.1175/JAS-D-13-0219.1.
- Parker, M. D., 2012: Impacts of lapse rates on low-level rotation in idealized storms. *J. Atmos. Sci.*, **69**, 538–559, doi:10.1175/JAS-D-11-058.1.
- Rasmussen, E. N., and D. O. Blanchard, 1998: A baseline climatology of sounding-derived supercell and tornado forecast parameters. *Wea. Forecasting*, **13**, 1148–1164, doi:10.1175/1520-0434(1998)013<1148:ABCOSD>2.0.CO;2.
- Richardson, Y. P., P. M. Markowski, S. Waugh, and S. E. Fredrickson, 2010: Mobile mesonet observations during VORTEX2. *25th Conf. on Severe Local Storms*, Denver, CO, Amer. Meteor. Soc., P6.4. [Available online at [https://ams.confex.com/ams/25SLS/techprogram/paper\\_176206.htm](https://ams.confex.com/ams/25SLS/techprogram/paper_176206.htm).]
- Romine, G. S., D. W. Burgess, and R. B. Wilhelmson, 2008: A dual-polarization-radar-based assessment of the 8 May 2003 Oklahoma City area tornadic supercell. *Mon. Wea. Rev.*, **136**, 2849–2870, doi:10.1175/2008MWR2330.1.
- Schenkman, A. D., M. Xue, and A. Shapiro, 2012: Tornadogenesis in a simulated mesovortex within a mesoscale convective system. *J. Atmos. Sci.*, **69**, 3372–3390, doi:10.1175/JAS-D-12-038.1.
- , —, and M. Hu, 2014: Tornadogenesis in a high-resolution simulation of the 8 May 2003 Oklahoma City supercell. *J. Atmos. Sci.*, **71**, 130–154, doi:10.1175/JAS-D-13-073.1.
- Shabbott, C. J., and P. M. Markowski, 2006: Surface in situ observations within the outflow of forward-flank downdrafts of supercell thunderstorms. *Mon. Wea. Rev.*, **134**, 1422–1441, doi:10.1175/MWR3131.1.
- Snook, N., and M. Xue, 2008: Effects of microphysical drop size distribution on tornadogenesis in supercell thunderstorms. *Geophys. Res. Lett.*, **35**, L24803, doi:10.1029/2008GL035866.
- Spehger, D. A., C. A. Doswell III, and G. J. Stumpf, 2002: The tornadoes of 3 May 1999: Event verification in central Oklahoma and related issues. *Wea. Forecasting*, **17**, 362–381, doi:10.1175/1520-0434(2002)017<0362:TTOMEV>2.0.CO;2.
- Stensrud, D. J., and Coauthors, 2009: Convective-scale warn-on-forecast system: A vision for 2020. *Bull. Amer. Meteor. Soc.*, **90**, 1487–1499, doi:10.1175/2009BAMS2795.1.
- , and Coauthors, 2013: Progress and challenges with warn-on-forecast. *Atmos. Res.*, **123**, 2–16, doi:10.1016/j.atmosres.2012.04.004.
- Straka, J. M., E. N. Rasmussen, and S. E. Fredrickson, 1996: A mobile mesonet for finescale meteorological observations. *J. Atmos. Oceanic Technol.*, **13**, 921–936, doi:10.1175/1520-0426(1996)013<0921:AMMFFM>2.0.CO;2.
- Thompson, R. L., R. Edwards, J. A. Hart, K. L. Elmore, and P. Markowski, 2003: Close proximity soundings within supercell environments obtained from the Rapid Update Cycle. *Wea. Forecasting*, **18**, 1243–1261, doi:10.1175/1520-0434(2003)018<1243:CPSWSE>2.0.CO;2.
- Xia, J., W. S. Lewellen, and D. C. Lewellen, 2003: Influence of mach number on tornado corner flow dynamics. *J. Atmos. Sci.*, **60**, 2820–2825, doi:10.1175/1520-0469(2003)060<2820:IOMNOT>2.0.CO;2.
- Xue, M., and Coauthors, 2001: The Advanced Regional Prediction System (ARPS)—A multi-scale nonhydrostatic atmospheric simulation and prediction tool. Part II: Model physics and applications. *Meteor. Atmos. Phys.*, **76**, 143–166, doi:10.1007/s007030170027.
- , D.-H. Wang, J.-D. Gao, K. Brewster, and K. K. Droegemeier, 2003: The Advanced Regional Prediction System (ARPS), storm-scale numerical weather prediction and data assimilation. *Meteor. Atmos. Phys.*, **82**, 139–170, doi:10.1007/s00703-001-0595-6.